

# Chapter1. Introduction

## 1-1. Background

In the development of modern technologies, the photonic technology is a novel category. This important category includes fiber communication, display device, optical information memory, and many kinds of passive and active devices, like light emission diode (LED), waveguide, and laser diode (LD), etc. With the advancement and breakthrough of research in photonic technology, it affects our life more and more and this trend will continue in the future.

Photonic crystal (PC) structure is established for these applications. The concept of photonic crystal was first proposed by Prof. Yablonovitch in 1987 [1]. It is formed by periodic variation in the refraction index or dielectric constant of materials. Figure1-1 shows three different photonic crystal structures.

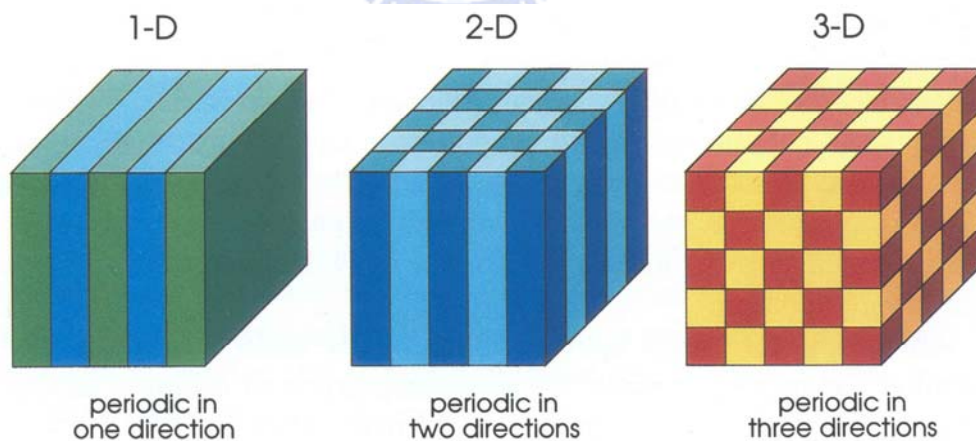


Figure1-1. The photonic crystals can be divided into one-, two-, and three-dimensional structures [2].

The PC structure is similar to the periodic atomic arrangement in the crystal. As in figure1-2, the photonic crystal structure will develop the photonic band gap just like the

electronic band gap of semiconductor. The principles of photonic crystal structures will be introduced in section1-3.

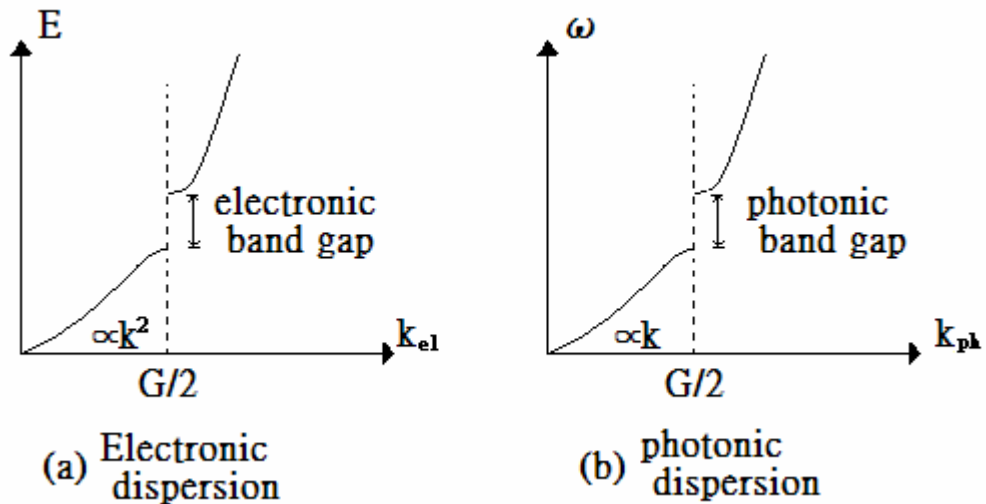


Figure1-2. The relations of (a) electronic dispersion and (b) photonic dispersion.

## 1-2. Research Motive

In the photonic crystal structure, the amplitude, phase, polarized direction, and wavelength of an electromagnetic wave all can be tuned by changing its structure. So it is easy to control light by photonic crystal structure especially when introducing a defect arrangement. There will be defect (guided) modes appeared in photonic band gap. The potential of application in many optical devices has attracted a lot of attention. The role of photonic crystals to light is like that of semiconductors to electrons.

The role of semiconductor laser diodes is more and more important since semiconductor laser diodes were first demonstrated in the early 1960's. They are used in wide applications such as readout source in optical disk media, biological detection, display, optical fiber communication, and optical computing, etc., due to the advantages of considerably smaller

size, higher efficiency with lower power requirements, long lifetime, and the ability to be modulated to a few GHz with a simple driving circuit.

My work is trying to combine the PC structure with semiconductor laser and focuses on the part of fabricating the photonic crystal laser devices. The ultimate goal will be trying to combine different kinds of optical devices all based on photonic crystal structures. It can be predicted that the world having integrated optical circuit will become true in the future.

### 1-3. Principles of Photonic Crystals

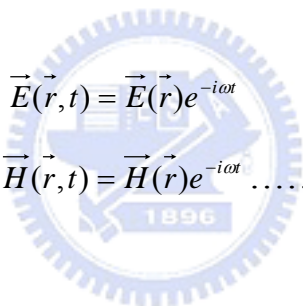
The motion of electronic wave in atomic crystal obeys Schrödinger equation:

$$\left[-\frac{\hbar^2}{2m^*}\nabla^2 + V(r)\right]\psi(r) = E\psi(r) \dots\dots\dots (1-1)$$

where  $m^*$  is the effective mass of electron,  $\psi(r)$  is the function of electronic wave,  $V(r)$  is the potential of crystal, and  $E$  is eigen-energy of electron. The motion of light in photonic crystal is described by Maxwell equations. In the conditions of no free electric charge and current the Maxwell equations can be written as:

$$\begin{aligned} \nabla \times \vec{E}(\vec{r}, t) + \mu_0 \frac{\partial \vec{H}(\vec{r}, t)}{\partial t} &= 0 \\ \nabla \times \vec{H}(\vec{r}, t) - \varepsilon(\vec{r})\varepsilon_0 \frac{\partial \vec{E}(\vec{r}, t)}{\partial t} &= 0 \\ \nabla \cdot [\varepsilon(\vec{r})\varepsilon_0 \vec{E}(\vec{r}, t)] &= 0 \\ \nabla \cdot \vec{H}(\vec{r}, t) &= 0 \dots\dots\dots (1-2) \end{aligned}$$

where  $\vec{r}$  is the vector of position,  $t$  is time,  $\vec{E}$  is the electric field,  $\vec{H}$  is the magnetic field,  $\epsilon_0, \mu_0$  is permittivity and permeability in free space, and  $\epsilon(\vec{r})$  is relative dielectric constant which is a function of position. The obvious difference to Schrödinger equation is that the Maxwell equations are vectored equations. So it is necessary to assign the polarized direction in any point of space. At first the Maxwell equations are not independent to each other. Two curl equations imply two divergent equations. Generally we only need to solve the curl equations and the divergent equations will be satisfied spontaneously. We can choose the electric field or magnetic field to be the independent variable. For the convenience of calculation, we often choose the magnetic field as the independent variable. We assume that



$$\begin{aligned}\vec{E}(\vec{r}, t) &= \vec{E}(\vec{r})e^{-i\omega t} \\ \vec{H}(\vec{r}, t) &= \vec{H}(\vec{r})e^{-i\omega t} \dots\dots\dots (1-3)\end{aligned}$$

Substitute equation(1-3) into Maxwell equations and cancel the factor of time  $e^{-i\omega t}$ , the new Maxwell equations are as follows:

$$\begin{aligned}\nabla \times \vec{E}(\vec{r}) &= i\omega\mu_0\vec{H}(\vec{r}) \\ \nabla \times \vec{H}(\vec{r}) &= -i\omega\epsilon_0\epsilon(\vec{r})\vec{E}(\vec{r}) \\ \nabla \cdot [\epsilon(\vec{r})\vec{E}(\vec{r})] &= 0 \\ \nabla \cdot \vec{H}(\vec{r}) &= 0 \dots\dots\dots (1-4)\end{aligned}$$

The next step is to cancel the electric field  $\vec{E}(\vec{r})$  and obtain the magnetic field  $\vec{H}(\vec{r})$  which satisfies

$$\nabla \times \left( \frac{1}{\epsilon(\vec{r})} \nabla \times \vec{H}(\vec{r}) \right) = \frac{\omega^2}{c^2} \vec{H}(\vec{r}) \dots\dots\dots(1-5)$$

where  $c = (\mu_0 \epsilon_0)^{-1/2}$  is the velocity of light in free space. After the magnetic field is obtained, the corresponding electric field  $\vec{E}(\vec{r})$  is

$$\vec{E}(\vec{r}) = \left( \frac{i}{\omega \epsilon(\vec{r}) \epsilon_0(\vec{r})} \right) \nabla \times \vec{H}(\vec{r}) \dots\dots\dots (1-6)$$

Notice that equation(1-5) is an eigen-value problem. It means that the solution  $\vec{H}(\vec{r})$  corresponds to the eigen vector of a linear operator  $\Theta$ , which is

$$\Theta = \nabla \times \left( \frac{1}{\epsilon(\vec{r})} \nabla \times \right) \dots\dots\dots (1-7)$$

Equation(1-5) also can be written as the simple form of

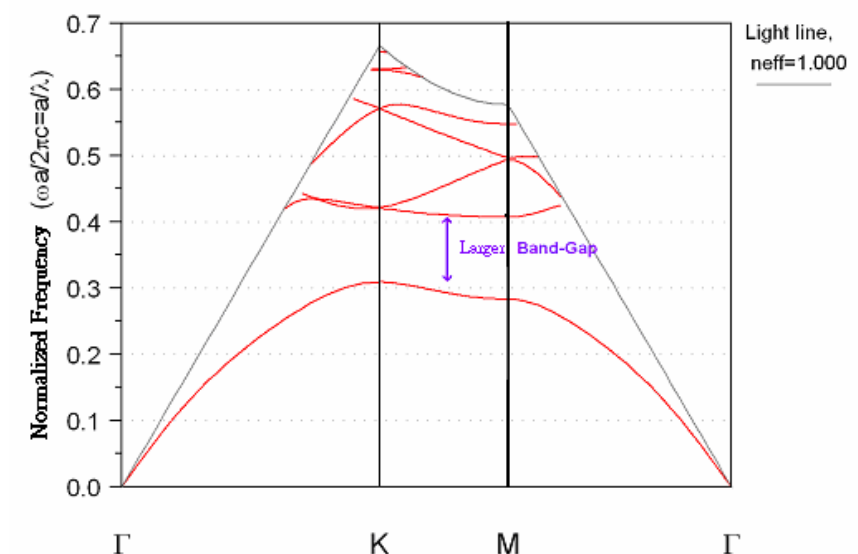
$$\Theta H(r) = \frac{\omega^2}{c^2} H(r) \dots\dots\dots(1-8)$$

where the ratio  $\frac{\omega^2}{c^2}$  is the eigen-value. It can be proven that the linear operator  $\Theta$  is a self-adjoint operator. By this reason the eigen-values must be real numbers. The set of eigen-values which corresponds to all non-zero eigen-vectors composes the band structure. It also can be called as the dispersion relation.

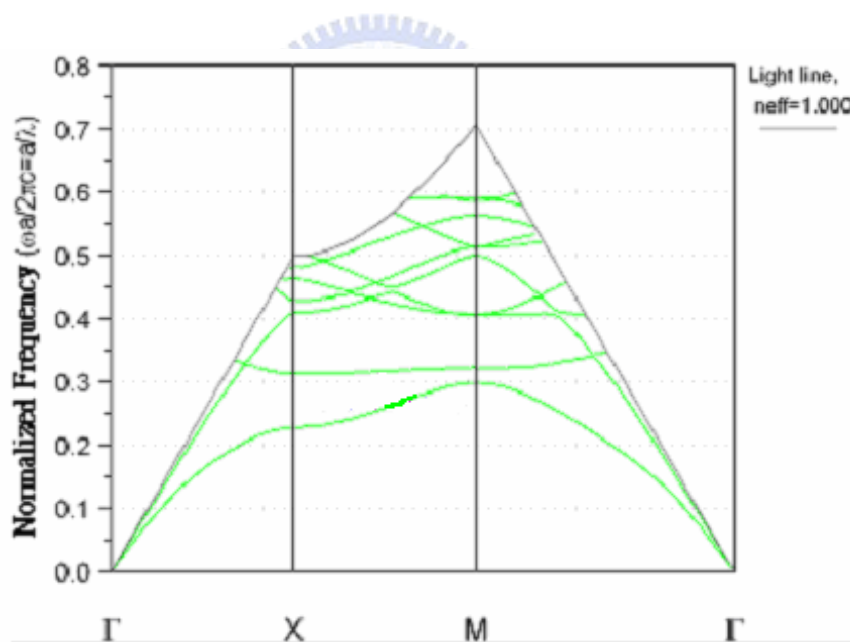
## 1-4. History and Developments

In 1999, two-dimensional (2D) photonic crystal lasers were first demonstrated by O. Painter et al. at Caltech [3]. They are potential light sources in optical communication systems due to several advantages such as ultra-low threshold, small mode volume, and high quality (Q) factor. More and more photonic crystal lasers were reported in recent years. In this section, I will introduce the history and developments of photonic crystal micro-cavity lasers briefly.

The photonic crystal micro-cavity lasers with triangular lattice [4, 5] and square lattice [6, 7] have been widely investigated. The triangular lattice photonic crystal lasers are much easier to be demonstrated than the square lattice photonic crystal lasers because of the larger band-gap. This can be easily shown by using 3D plane-wave expansion method (PWE) to calculate the corresponding photonic band structures as shown in figure1-4-1(a) and (b). There is no complete band gap for square lattice structures with the same lattice parameters, so there is still inevitably optical loss along some crystal directions. But square lattice structure still has advantages like the tightly confinement of light and can be a good candidate for low-threshold photonic crystal lasers with small mode volume due to the presence of lowest whisper-gallery-mode [8]. Moreover, this mode has a node for both electric and magnetic fields at the center that can be conveniently used for electrical current pumping.



(a)



(b)

Figure1-4-1. The typical TE-like band diagrams of photonic crystal slabs with (a) triangular lattice and (b) square lattice. The band-gap of triangular lattice is much larger than that of square lattice with the same lattice constant and  $r/a$  ratio.

Researchers focus on improving different characteristics of 2D photonic crystal lasers such as ultra-low threshold, high Q factor, high side mode suppression ratio, high  $\beta$  value, and small mode volume. In order to obtain better characteristics of photonic crystal lasers, more and more researchers focus on the modification of photonic crystal patterns including mismatching of the surrounding photonic crystal and shrinking of the air-holes near the micro-cavity [10-12]. A lot of excellent ideas have been reported in recent years. But one of the main problems for this lower-than-expected efficiency is the surface recombination of carriers at low carrier densities. Recently, by limiting the surface recombination by the introduction of the quantum-dot active material, over a 30-fold increase in extraction efficiency is reported [13]. In fact, this value demonstrates more than 90% net extraction of photons from the high-index semiconductor materials.

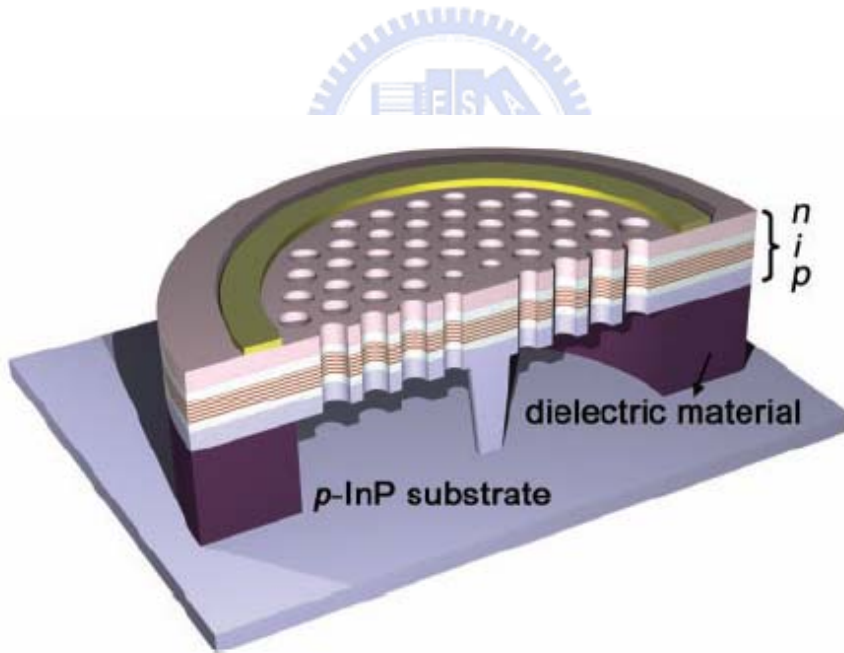
One noticeable advantage of the photonic crystal is its forgiveness against the critical fabrication. For example, each of the holes of the lattice does not have to be extremely uniform. Even with some irregularities in size and shape, the major properties of the photonic band gap remain almost unchanged except the region near the band edge [14]. The electromagnetic waves interact with a periodic structure over a long range, thereby some kind of nature averaging takes place in the photonic crystal.

At last, most of these photonic crystal lasers reported in recent years are under pulsed operation due to lack of heat sink. This is caused by the low thermal conductivity of the air claddings in the generally-used structure. As a result, the high index contrast structures often lead to a low thermal conductivity. There is a big problem for the improvement towards continuous-wave operation and electrical injection for devices in the future. Although the

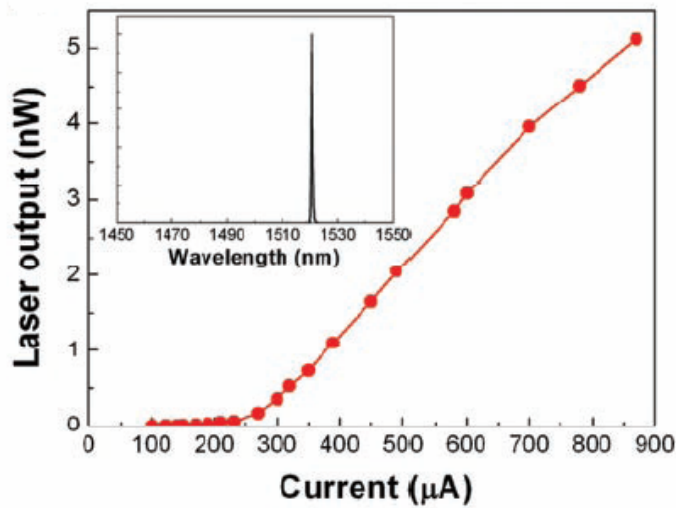


continuous-wave operation of photonic crystal lasers had been reported, the size of these cavities was still quite large [15, 16].

In addition, the serious surface recombination of photonic crystals and the proper micro-cavity structures should be solved to achieve the goal of electrical injection. There are more and more excellent ideas proposed. In 2004, the first electrical-driven single defect photonic crystal micro-cavity laser with ultra-high  $\beta$  value and lower threshold than the general VCSELs was demonstrated by H.-G. Park et al [17]. This electrically-driven device is shown in figure1-4-2 (a) and (b). This is a great improvement in the technologies of photonic crystal micro-cavity lasers. And it is believed that there will be more and more excellent achievements in the future.



(a)



(b)

Figure1-4-2. (a) The illustration of the structure with central post for an electrically-driven single defect photonic crystal micro-cavity laser.  
 (b) The L-I curve of this photonic crystal laser.

## 1-5. Thesis Overview

In this thesis the fabrication of photonic crystal membrane lasers is presented in chapter2. Wafer bonding technology is introduced in chapter3 to integrate photonic crystal cavity wafer with different incompatible wafers. Chapter4 shows the instruments of measurement and the results of simulation and measurement for our devices. Chapter5 is the conclusions of this thesis.

## Chapter2. Fabrication of Membrane Structures

### 2-1. Research Motive

In two-dimensional photonic crystal laser structures, in order to confine light in the vertical direction and decrease the optical loss, the index contrast of materials should be enlarged. The method we use is to make a membrane structure to optimize the vertical confinement and then we can focus on the in-plane confinement issues. The membrane structure device is shown in figure2-1-1 [18-20].

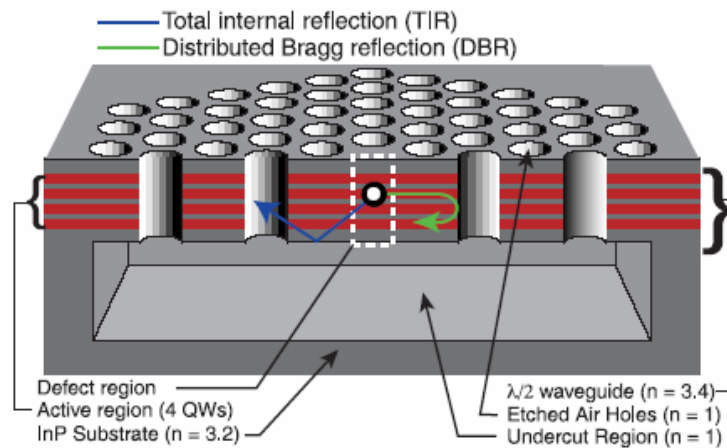


Figure2-1-1. The basic structure of a two-dimensional photonic crystal membrane laser.

The photonic crystal pattern is introduced to the laser device to provide the in-plane confinement. The resonant cavity is formed by introducing a defect pattern. Due to the excellent confinement for the defect mode, the threshold power can be lower than that of the traditionally material-cladding structure. As a result, the membrane structure of photonic crystal laser is the essential structure for an ideal device.

## 2-2. Fabrication of Two-Dimensional Photonic Crystal Lasers

The membrane structure devices are fabricated in the material system with an active layer of four compressively strained InGaAsP QWs separated by three unstrained InGaAsP barriers, as shown in figure2-2-1. The peak emission wavelength is at 1550 nm and the epitaxy is designed so that a 220nm thickness membrane will be formed by undercut of InP substrate layer [21]. The process of device is separated into four steps as follow:

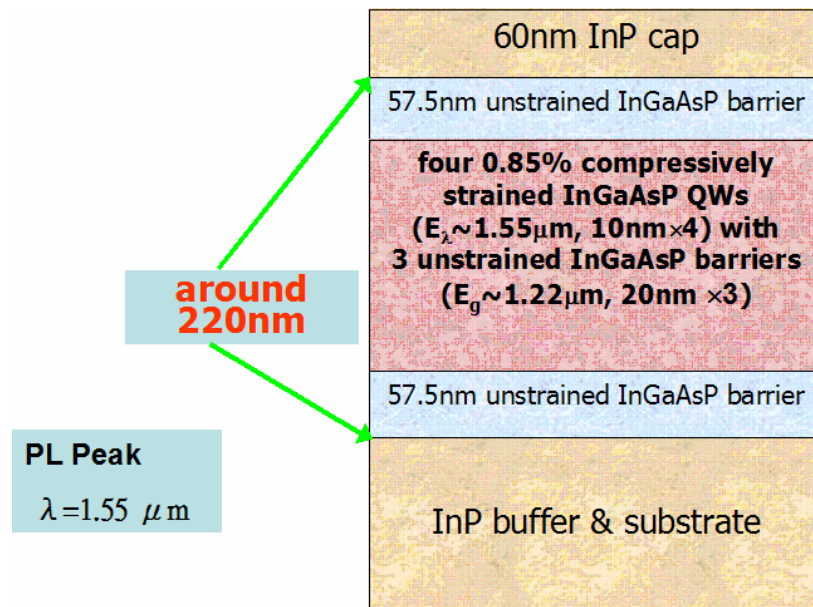


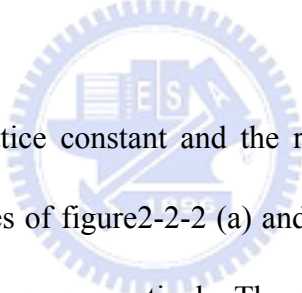
Figure2-2-1. The membrane epitaxial structure.

### 2-2-1. Dielectric mask deposition

In the first step the Si<sub>x</sub>N<sub>y</sub> layer with a thickness of 140 nm is deposited on the InP cap layer by Plasma Enhanced Chemical Vapor Deposition (PECVD) system with a mixture of SiH<sub>4</sub>/NH<sub>3</sub>/N<sub>2</sub>. The thickness of Si<sub>x</sub>N<sub>y</sub> layer is chosen to sustain the later deep etching of InGaAsP/InP active layer, taking into account the InP/Si<sub>x</sub>N<sub>y</sub> etch selectivity and allowing for an etch lag in deep holes.

### 2-2-2. Electron-Beam lithography (EBL)

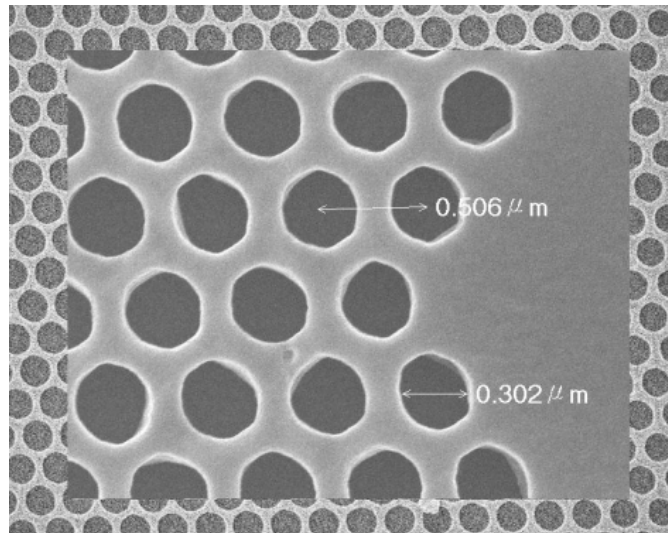
Two-dimensional triangular photonic crystal patterns are defined on a 240 nm polymethylmethacrylate (PMMA) using the EBL system. The thickness of PMMA-layer is chosen to enable the patterns transferred to the  $\text{Si}_x\text{N}_y$ -layer in the Reactive Ion Etching (RIE) process, accounting for the  $\text{Si}_x\text{N}_y$ /PMMA etch selectivity and allowing for an etch lag in small-diameter holes. After a series of development and fixation, the top view scanning electron microscopy (SEM) pictures of the photonic crystal patterns are shown in figure2-2-2. Besides the thickness of PMMA layer, the effect factor of EBL process is electron dosage. The proper dosage should be tested and chosen before the PMMA layer is exposed by electron-beam. Here is a simple experiment to confirm the influence of dosage.



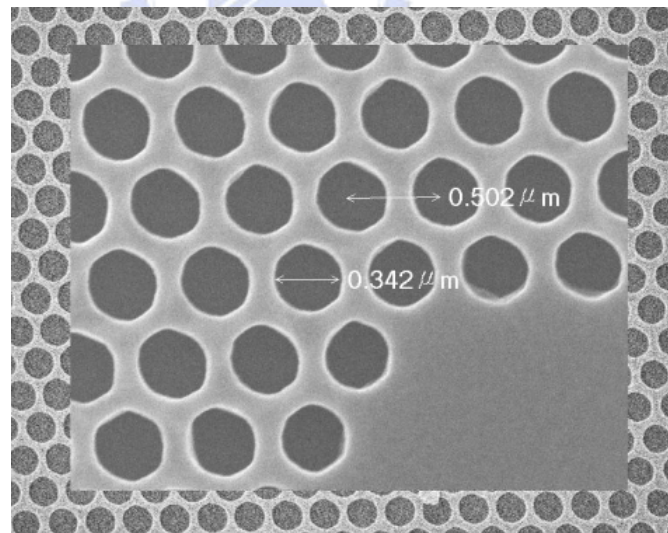
In the experiment, the lattice constant and the radius of air holes are designed to be 500nm and 160nm. The dosages of figure2-2-2 (a) and (b) are 1.4 fC and 1.6 fC, correspond to underexposure and overexposure, respectively. The radius of air holes with 1.4 fC dosage is smaller than the originally designed dimension due to underexposure. The radius of air holes is enlarged for 1.6 fC dosage and the degree of enlargement is about 10 nm. But the smoothness of air-hole edges of these two recipes is not good enough.

The dosages in figure2-2-2(c) and (d) are 1.8 fC and 2.1 fC, respectively. The enlarged radii of holes due to overexposure are about 20 and 40 nm. The smoothness of air-hole edges of figure2-2-2(c) is better than that of figure2-2-2(b) and the best uniformity for smoothness is dosage 2.1 fC in figure2-2-2(d). This fabrication variation should be considered in our designs. It is inevitable to have some overexposure of air holes in order to reduce roughness to prevent

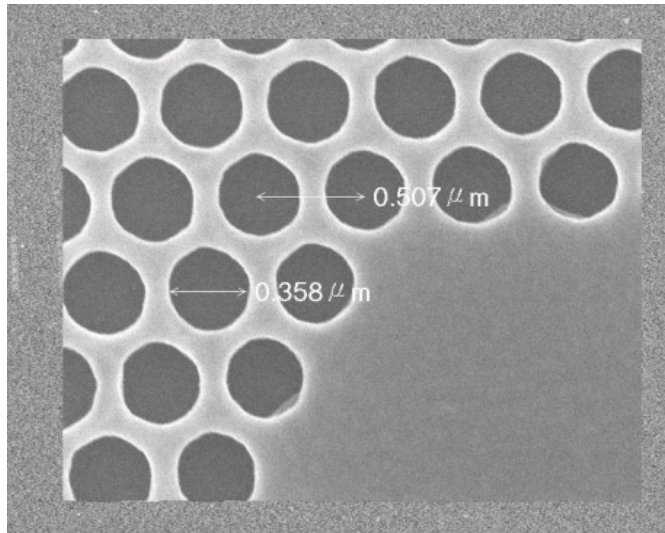
the optical loss. The way to solve this problem is to consider the degree of enlargement and design smaller air-hole sizes in advance or define every possibly suitable dosed patterns. For our devices the 1.6 fC and 1.8 fC dosages are practiced.



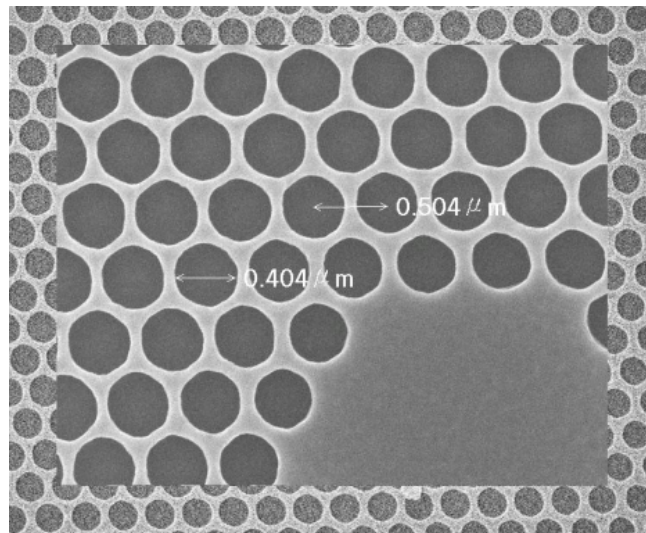
(a)



(b)



(c)



(d)

Figure2-2-2. The top view SEM pictures with (a) 1.4 fC, (b) 1.6 fC, (c) 1.8 fC, and (d) 2.1 fC dosages in EBL process.

The top view SEM picture of the photonic crystal pattern defined on PMMA-layer with 500 nm lattice constant and 100 nm air-hole radius is shown in figure2-2-3. But the real air-hole radius measured is 120 nm with 1.8 fC dosage. Therefore, we can obtain the dimension we want by taking the fabrication variation into consideration in our designs. In order to reduce the roughness of air holes, the quantity of exposure is overdosed intentionally

but the dimensions of air holes still can be controlled. So we can assume that only EBL process can affect the air hole dimensions and ignore the influence by the later RIE and Inductive Coupled Plasma (ICP) processes.

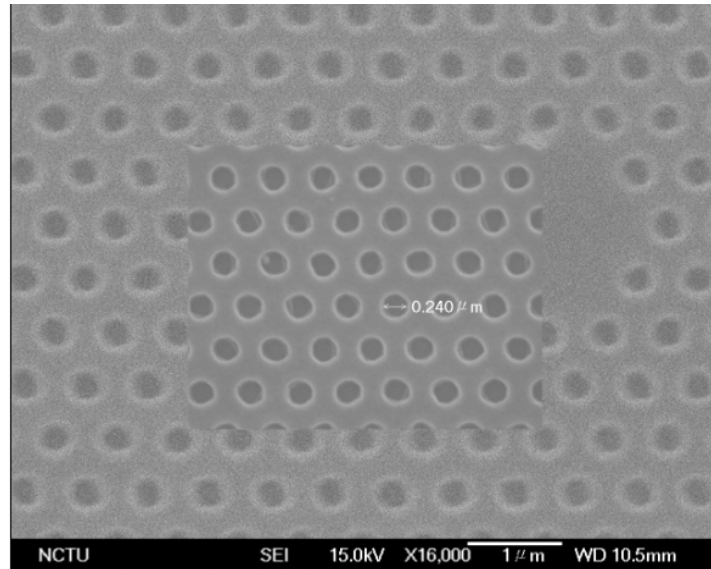


Figure2-2-3. The top view SEM picture of photonic crystal patterns defined on PMMA layer.

### 2-2-3. RIE/ICP dry etching

An Oxford Instruments Plasma Technology Plasmalab system 100 RIE/ICP is used in order to transfer the PMMA patterns to  $\text{Si}_x\text{N}_y$  layer and etch through the InGaAsP membrane layer into the InP substrate with  $\text{Si}_x\text{N}_y$  layer as mask [22]. The selectivity of InP to  $\text{Si}_x\text{N}_y$  material in dry etching process is 6. And the etching rate depends on the power used.

In etching process the first step is to etch  $\text{Si}_x\text{N}_y$  for transferring the patterns to  $\text{Si}_x\text{N}_y$  layer using RIE with reactive gases  $\text{CHF}_3/\text{O}_2$  and power 150W. The substrate temperature is fixed at  $20^\circ\text{C}$  and the etching rate is 90nm/min. The second step is 10-minute  $\text{O}_2$  plasma for the chamber cleaning (unload wafer). The final step is to transfer patterns to InGaAsP/InP (>300nm) active layer. The ICP system is used with reactive gases  $\text{H}_2/\text{CH}_4/\text{Cl}_2$ , and the



substrate temperature is fixed at 150°C. The etching rate is 330nm/min, and in order to maintain the integrity of the ICP/RIE chamber, the O<sub>2</sub> plasma clean step is periodically run between each etching step. The patterns after RIE/ICP etching process are shown in figure2-2-4.

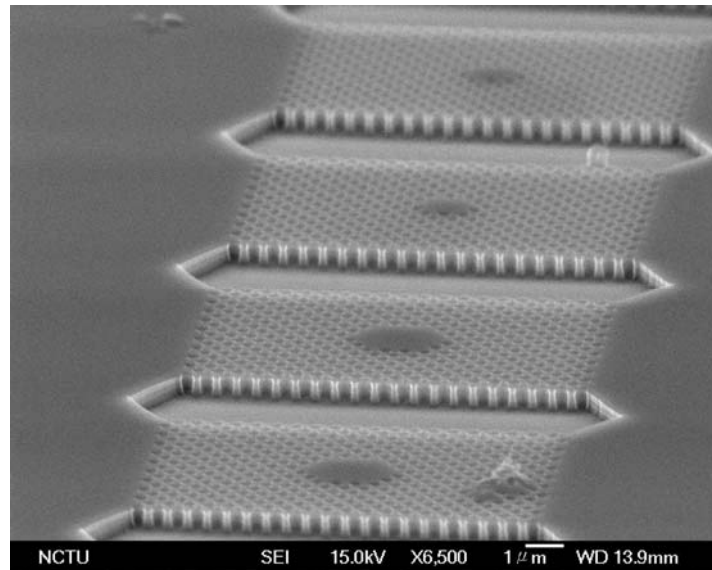
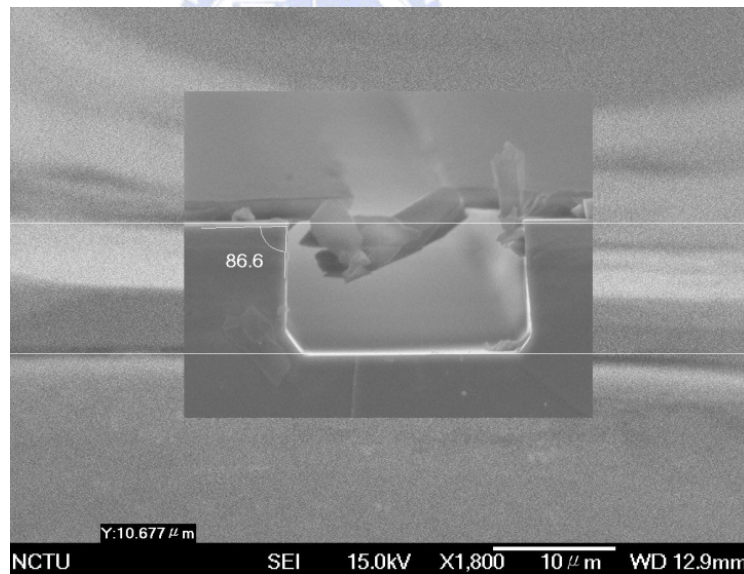


Figure2-2-4. The SEM picture of devices after ICP process.

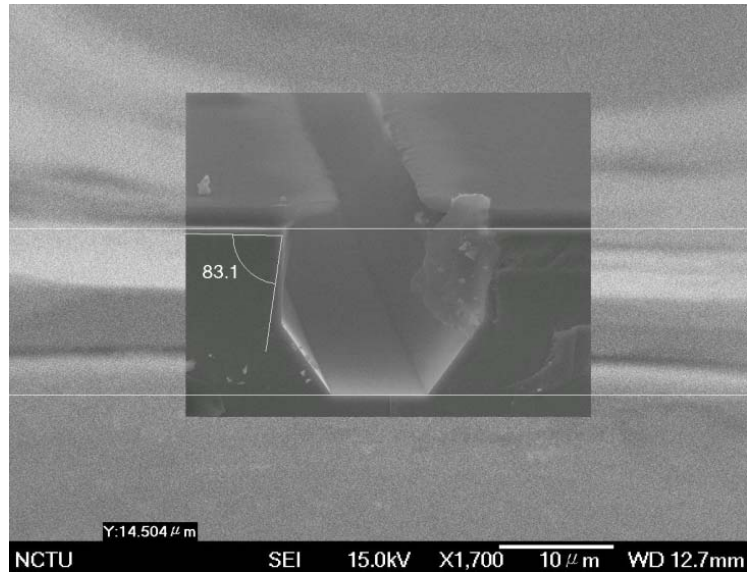
#### **2-2-4. InP substrate undercut**

The last step is to undercut the membrane structure and a HCl : H<sub>2</sub>O = 4 : 1 solution is used. The HCl solution etches the InP layer at a faster rate than it does the InGaAsP active layer, providing the necessary degree of etch selectivity. This process also smoothes most of the sharp features on the sidewalls of the holes, which decreases the optical loss caused by the roughness. The wet etching is executed at 2°C for 8 minutes. The resolution and selectivity of the etching are improved by cooling the solution.

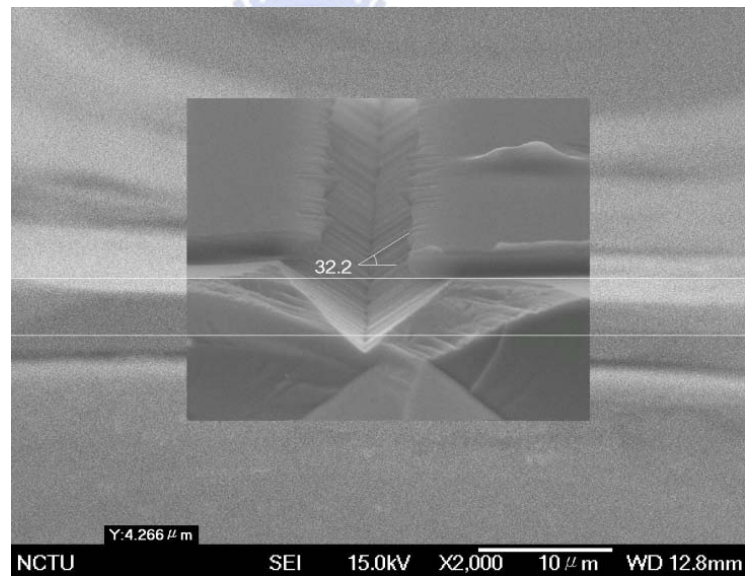
The consequence of anisotropic etching is shown in figure2-2-5. Here we use the  $\text{Si}_x\text{N}_y$  layer with 140 nm as a hard mask on the InP substrate. The (a), (b) of figure2-2-5 both show that the HCl etching effectively stops at about the angle of  $85^\circ$ , and (c) stops at the angle of  $32.2^\circ$ , respectively. The channels in (a) and (b) are along the  $\langle -1, 0, 0 \rangle$  direction in the  $(0, -1, -1)$  plane, for convenience we call this etching profile U-shape. Figure2-2-5(a) and (b) show the different etching time for 6 and 8 minutes, respectively. The channel in (c) is the  $(0, 1, -1)$  plane [23, 24] along the same direction, which we call the V-shape profile. The etching depth is determined by the V-shape direction. The etching depth of U-shape channel increases with the etching time, but it will also stop at somewhere deeper. The property of U-shape is beneficial to the process of membrane structure.



(a)



(b)



(c)

Figure2-2-5. These are the etching profiles of InP material along  $\langle -1, 0, 0 \rangle$  direction in the  $(0, -1, -1)$  plane with etching time (a) 6, (b) 8 minutes, and (c) in the  $(0, 1, -1)$  plane with 8 minutes.

Due to the anisotropic property of HCl wet etching in InP material, the window patterns between devices are designed for undercut process. They are designed to align along the

U-shape direction. After the undercut step, along the  $\langle -1, 0, 0 \rangle$  direction, the air holes can be tunneled with each other side by side. And because of the introducing of window patterns, the array of the membrane structure devices can be demonstrated.

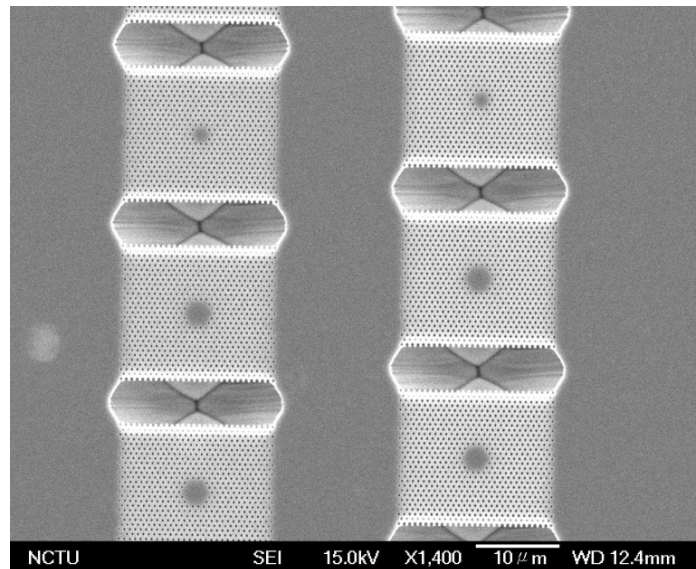


Figure2-2-6. The top view of devices after failed undercut process.

Figure2-2-6 shows the top view of devices after undercut process. The photonic crystal patterns in figure2-2-6 present the failed etching process. If the sample is only immersed in the stable solution, the etching corpuscles will remain at the area of window patterns. A magnetic agitator must be employed to make the etching process become successful. If the undercut process is failed, the V-shape of air holes will appear as in figure2-2-7. When the V-shape of air holes is formed, the undercut process becomes impossible to succeed because the etching has already stopped. Figure2-2-8(a) and (b) show another failed result of undercut process and a successful result.

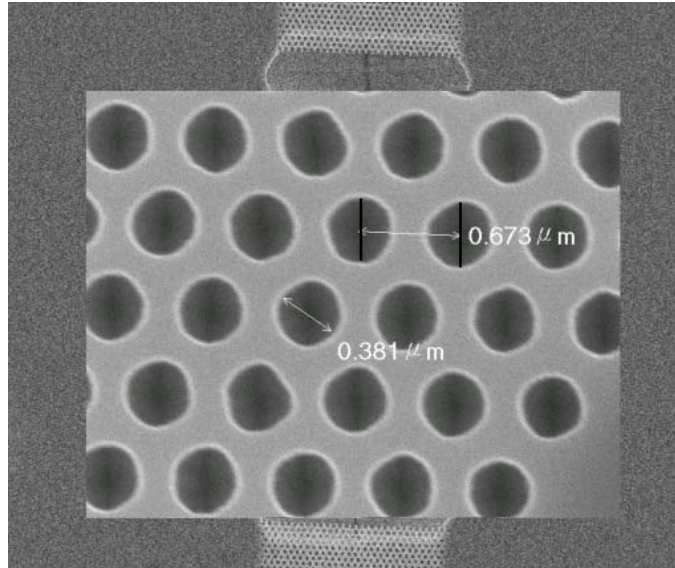
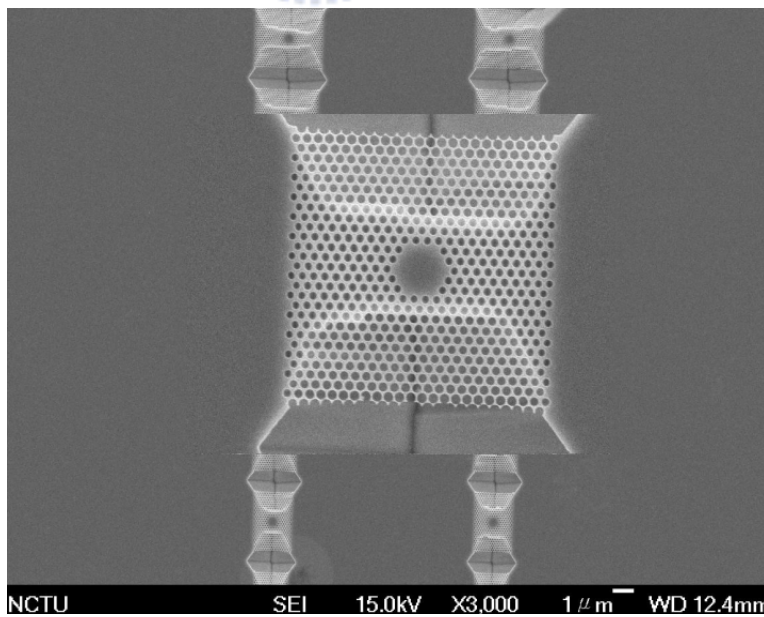
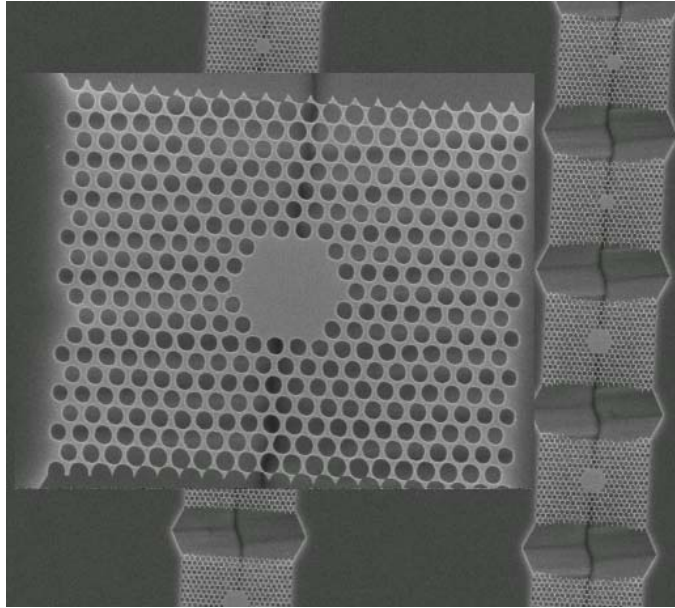


Figure2-2-7. The V-shape patterns appear in the center of air holes and this means that the undercut process is failed.



(a)



(b)

Figure2-2-8. The top view SEM pictures of two-dimensional photonic crystal micro-cavities after (a) failed and (b) successful undercut processes.

Figure2-2-9 shows the tilted view of complete devices. The membrane structure can be observed and the thickness of the photonic crystal membrane is 220nm.

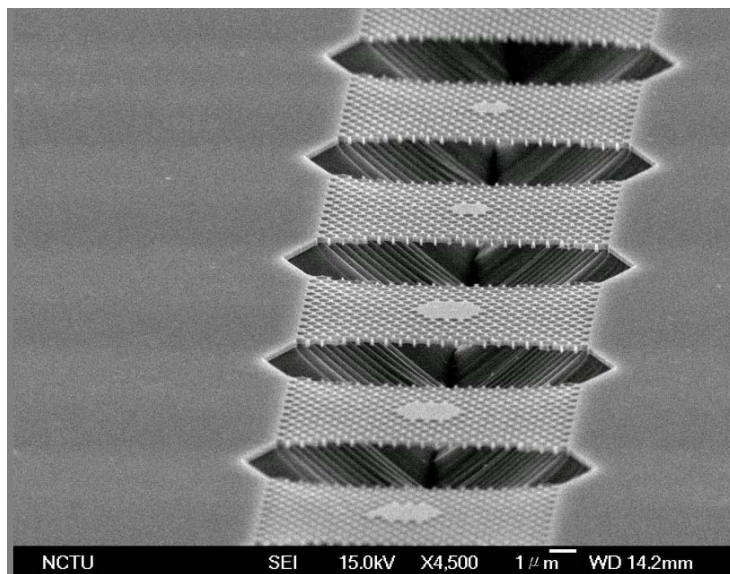


Figure2-2-9. The tilted view SEM picture of two-dimensional photonic crystal membrane structure.

## 2-3. Conclusions

The complete process flow of 2D photonic crystal membrane lasers is shown in figure2-3-1. Besides the recipe of solution, temperature of solution, and accurate alignment of patterns, the most important factor in undercut process is  $r/a$  ratio. The  $r/a$  ratios of photonic crystal patterns designed are from 0.2 to 0.32. The samples which have larger  $r/a$  ratio are much easier to be fabricated. Here the  $r/a$  ratio of membrane devices successfully fabricated is from 0.26 to 0.32. There is still potential to improve the fabrication process to decrease the  $r/a$  ratio.

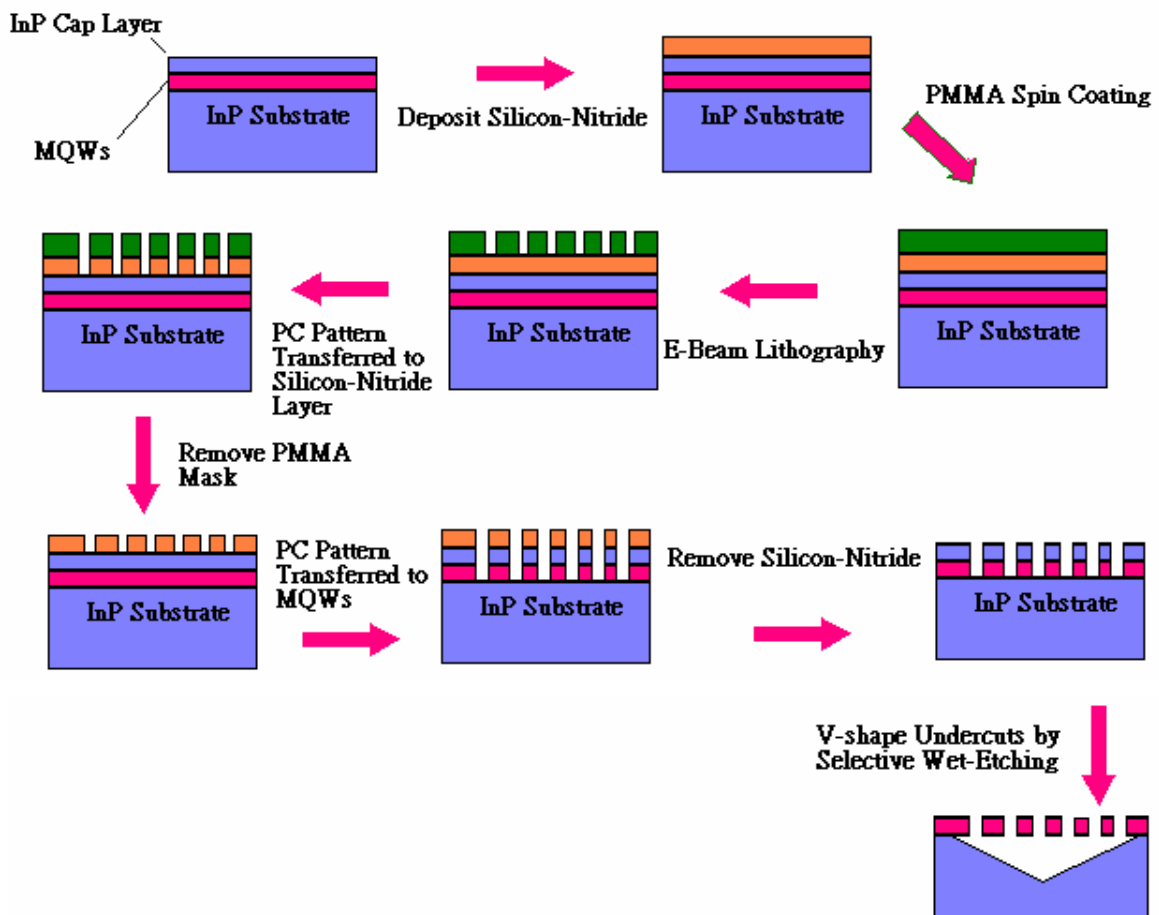


Figure2-3-1. Fabrication procedure of two-dimensional photonic crystal membrane lasers.

## Chapter3. Wafer Bonding Technology

### 3-1. Introduction

In recent years, wafer bonding technology [25] has been applied to integrate many different materials. It is employed at optoelectronic integrated circuits (OEICs), high brightness light emission diodes (LEDs) [26], vertical cavity surface emitting lasers (VCSELs) [27], poly-silicon thin film transistors (TFTs) [28], and nonlinear optical devices [29]. In the traditional technology of epitaxial growth like metal organic chemical vapor deposition (MOCVD), for example, the lattice mismatch between different semiconductor layers often leads to high-density threading dislocation [30-32]. And it affects seriously the performance of devices. Wafer bonding technology is a good method to integrate wafers with different lattice constants or crystal directions [33] in which cases we can't use MOCVD to grow. Wafer bonding technology can satisfy various designs of devices and increase the degree of integration in multiple devices. As a result, smaller and more versatile devices can be realized.

### 3-2. Research Motive

The properties of the materials used in a laser structure are the key issue in the fabrication of a laser diode. The most fundamental requirements for these different materials are the same crystal structure and nearly the same lattice constant. Therefore, single crystal and defect free films can be epitaxially grown on each other.

Figure3-2-1 shows the energy band gap vs. lattice constant for several III-V compounds [34]. As shown in figure3-2-1, the lattice constants of InP and GaAs are 5.86 Å and 5.65 Å, respectively. It is well known that a small lattice mismatch ( $\Delta a/a \sim 1\%$ , where  $a$  is the lattice



constant and  $\Delta a$  is the difference of lattice constants between the two materials) can be tolerated up to a critical thickness of about 20nm without any defect. The  $\Delta a/a$  ratio of InP/GaAs is about 3%, therefore the critical thickness must be thinner than 20 nm. The thin thickness limits probable application of GaAs epitaxial grown on InP. In this thesis, wafer bonding technique is used to overcome the lattice-mismatched problem.

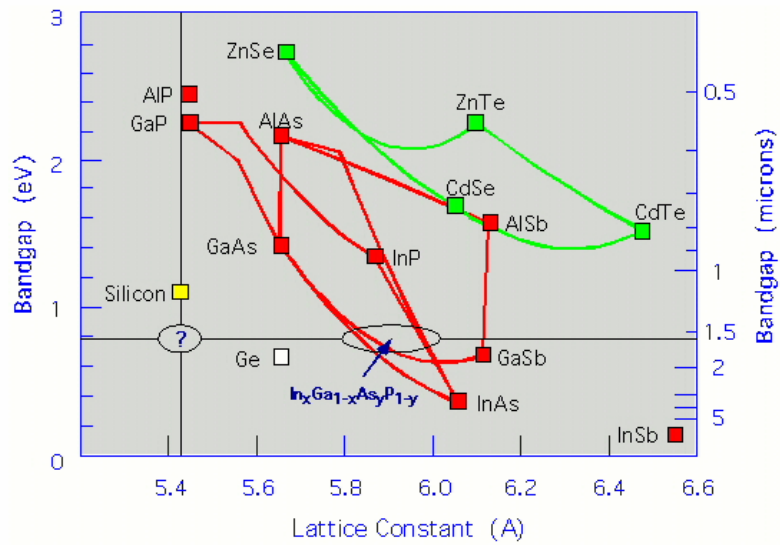


Figure3-2-1. Relation between energy band gap and lattice constant for several III-V compounds.

For the photonic crystal lasers, in order to optimize the performance of devices, we have to integrate photonic crystal cavity wafer with different kinds of materials as the substrates. Here two cases are investigated. One is MQWs bonded to DBR and the other is bonded to sapphire.

### 3-2-1. Bonding to DBR

The in-plane light confinement of a PC laser is provided by the photonic crystal structure. For the vertical direction, the confinement of light is determined by the index contrast of

materials. In order to optimize the confinement of light in vertical direction, air or substrate with low refractive index should be employed. In addition, DBR structure also can be utilized. Figure3-2-2 shows the reflectance as a function of wavelength for a DBR. Here the DBR is composed of 22 pairs of GaAs and  $\text{Al}_{0.9}\text{Ga}_{0.1}\text{As}$  layers. Because the lattice constant of GaAs mismatch that of InP, the wafer bonding technology is applied to solve this problem. The reflectance of DBR can be up to 99.5% for the wavelength range from 1450 to 1600 nm. So it can be predicted that the device should have a characteristic of low threshold due to the low optical loss in vertical direction.

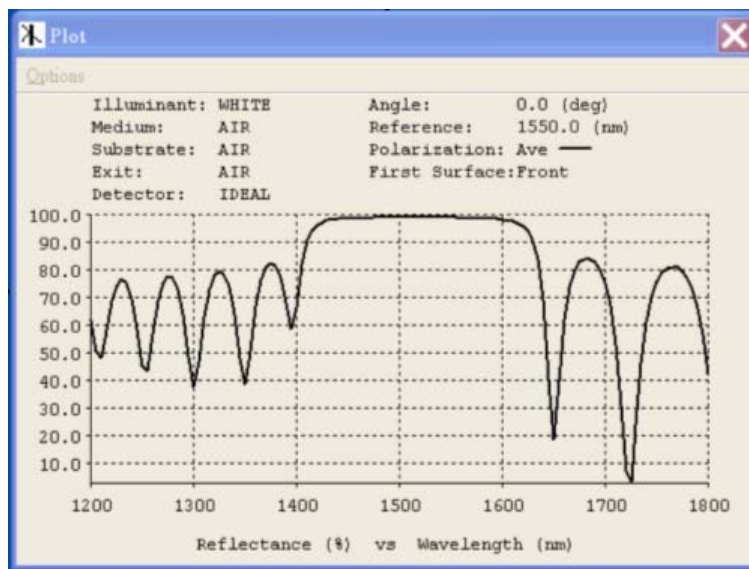


Figure3-2-2. The reflectance of DBR can be up to 99.5% for the wavelength range from 1450 to 1600 nm.

The structure of DBR has been applied to VCSEL devices for a long time. It acts as a mirror for a resonant cavity. The DBR structure can also be thought as a 1D photonic crystal structure. So in this topic the complete device can really be a device which has a pure photonic crystal structure.

### 3-2-2. Bonding to Sapphire

One of the problems for photonic crystal lasers is thermal effect. It can result in high threshold and the red shift of wavelength. Most of photonic crystal lasers only can be driven by pulsed pumping light. And it is a big challenge to pump with continuous-wave laser and even with the electric injection. Hence, the thermal conductivity of substrate is also an important factor to our devices.

Table3-2-1 shows the thermal conductivities and refractive indices of different materials and supplies us ideas for better characteristics of our laser devices. We use wafer bonding technology to integrate DBR/sapphire with the active layers of our devices.

Table3-2-1. Thermal conductivities and refractive indices of different materials.

Material	Si	Sapphire	Cu	GaAs	Al <sub>0.9</sub> Ga <sub>0.1</sub> As	InP
Thermal conductivity (W/cm°C)	1.3	0.35	3.937	0.55	0.65	0.68
Refractive index	3.42	1.77	2.43	3.3	2.9	3.1

From table3-2-1, silicon and copper are good choices to be the substrate materials of our devices due to their high thermal conductivities. But the problem is that the refractive index contrast with InP material is too small. It makes the optical loss too large in vertical direction. So there is a trade-off between optical loss and thermal effect. Here we choose sapphire as the

substrate of our devices to improve the thermal effect and minimize vertical optical loss. Figure3-2-3 shows the illustration of a sapphire-bonding PC laser cavity. The phenomenon of blue shift in wavelength after sapphire-bonding will be presented in chapter4.

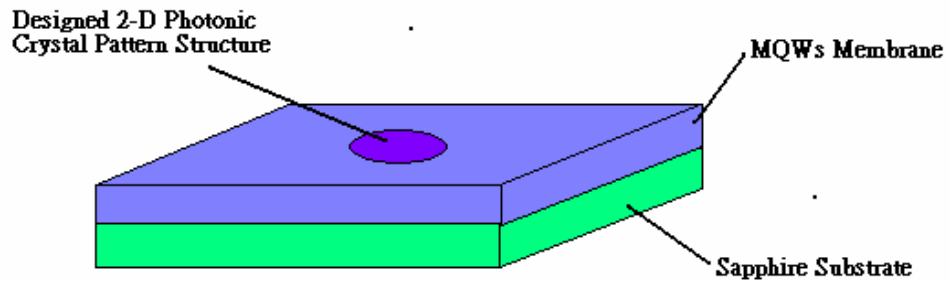


Figure3-2-3. A simple illustration of a two-dimensional photonic crystal laser cavity with asymmetric structure where the substrate is replaced by sapphire for better thermal conductivity.

### 3-3. Various Wafer Bonding Methods

In general, the wafer bonding technology means the “direct bonding” method [35]. It makes two wafers combined together by the atomic covalent bonds and attains the sufficient bonding intensity. It also means that two wafers are not combined by any other mediums but only by the force of covalent bonds.

The wafer bonding technology also involves other methods like the methods of anodic bonding, intermediate layer bonding, and adhesive bonding. The major goal of these methods is to reduce the annealing temperature. High annealing temperature usually causes destroying effects like thermal stress and atomic re-diffusion, rearrangement, or re-diffusion between two bonding materials at the interface. The high temperature also makes the devices have a

non-ideal characteristic. The introductions to these methods are described in the following sub-sections.

### 3-3-1. Anodic Bonding

When two samples are semiconductor and the insulator which has free ions (example of sodium), the anodic bonding method can be employed. The operation principles of this method are contacting the anode with semiconductor and the cathode with insulator, as in figure3-3-1. Because the nonconducting property of interface, the spacing electric field is formed by assembled electric charges. This method is very important and popular in the fabrication of MicroElectroMechanical systems [36]. In order to assist the closer contact by the force of electrostatic field, the samples are usually heated to 400~450°C. But cracks can often be observed due to different thermal indices.

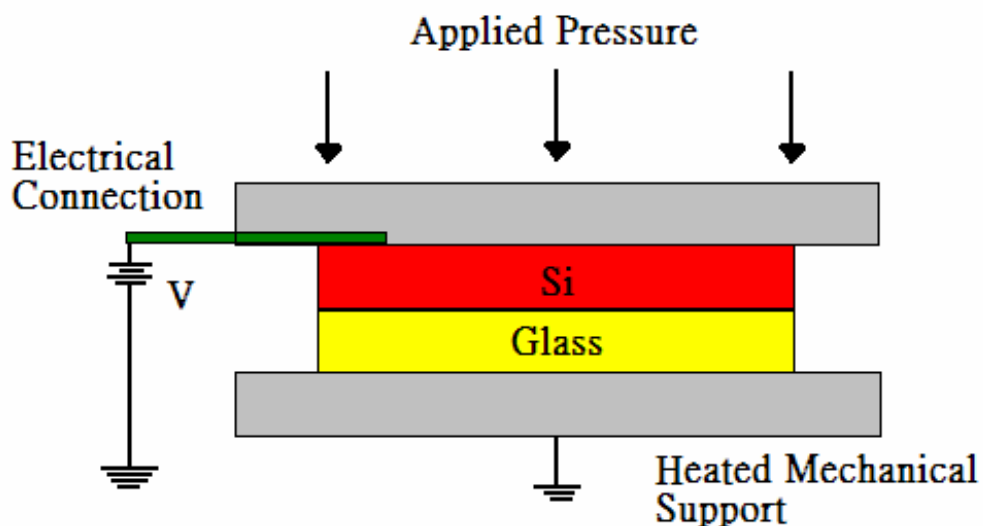


Figure3-3-1. The diagram of anodic bonding method.

### **3-3-2. Intermediate Layer Bonding**

This method spreads or sputters a layer of material which has the characteristics of high fluidity and low fusion point as an intermediate layer. It can decrease the annealing temperature but keep enough bonding strength. Examples are utilizing the spin-on-glass method to bond GaAs with Si [37] and utilizing the Indium (In) material as the intermedium for the fabrication of high brightness LEDs [38].

### **3-3-3. Low Temperature Bonding**

The wafer bonding process is usually practiced with an annealing procedure but this often affects the quality of samples especially for large-size samples. So it is a tendency to fabricate with low temperature process. The major key factors are introduced as follows.

#### **I. Enough Annealing Time**

Because the difference of thermal expansion indices between sapphire and Si is large, annealing temperature higher than 200°C is not allowed [39-40]. Low temperature process is practiced to prevent the appearance of thermal crack. But if we want to attain enough bonding strength, it is necessary to have longer annealing time. From figure3-3-2 [41], 3 hours are needed for the bond energy 1.2 J/m<sup>2</sup> at 200°C. But 10 hours are needed at 100°C to achieve the same bonding strength. So it can be predicted that the low-temperature process needs longer annealing time to have enough bonding strength.

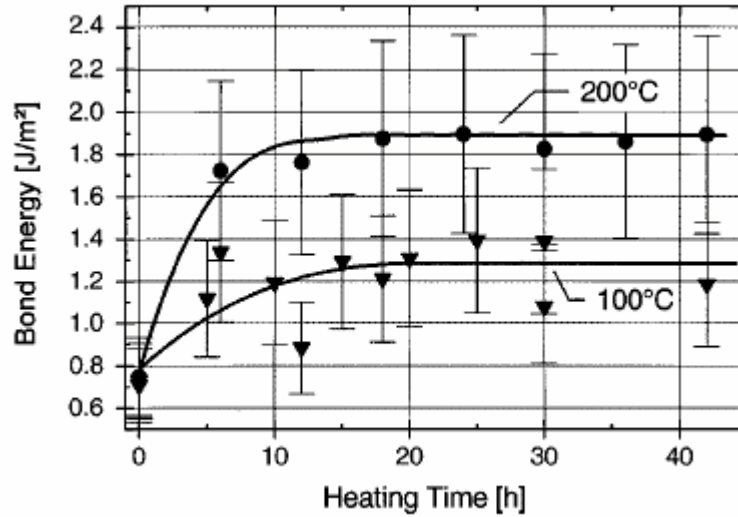


Figure3-3-2. The bond energy of Si on sapphire wafer.

## II. Bonding in High Vacuum

From figure3-3-3 [35], lower temperature is needed to reach the same bonding strength for the same annealing time in the high vacuum condition. It shows that the bonding strength in atmosphere condition at 1100°C can be easily achieved in high vacuum condition at 200°C. The possible reason is that in air bonding the density of void occupied by air at the interface is larger. As a result, the contact area is reduced and the density of covalent-bond atoms becomes smaller than in vacuum bonding.

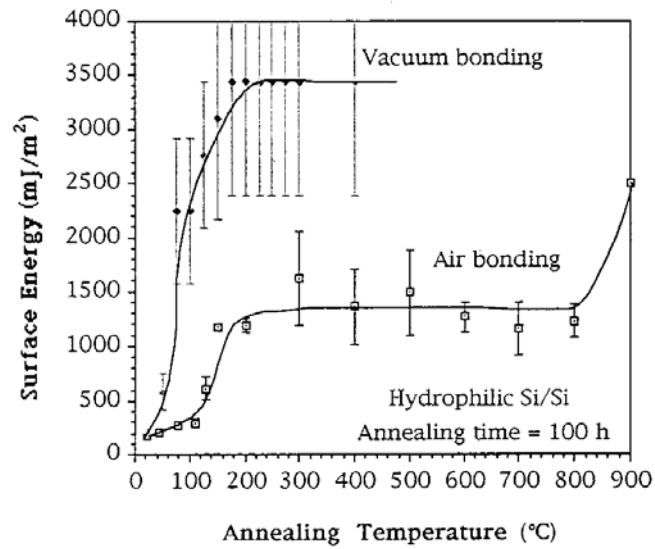


Figure3-3-3. The relation between annealing temperature and surface energy under different bonding atmospheres.

### III. Activation of Wafer Surface

The density of dangling bonds can be increased by the activation of wafer surface. The bonding strength of this method is close to the strength of nature materials. The generally-used activation method is plasma-activated bonding. The gas used is oxygen or argon [42].

#### 3-3-4. Direct Bonding

In this thesis, we apply the direct bonding method to fabricate our samples. The word “direct” means that two wafer surfaces are adhered to each other without any intermediate. The way to develop the covalent bonds is by using other external forces. The principles and process of the direct bonding method are accounted in section3-4.



### 3-3-5. Adhesive Bonding

This process utilizes organic-macromolecular-compound materials, such as photo resist, polymer, polyamide, epoxy, and so on, to adhere wafers [43]. The bonding temperature is about 120~140°C. But the bonding strength is smaller compared to other methods.

In this thesis, glue bonding is also practiced and the corresponding PL spectra of samples are measured. In our bonding experiments, the goal is to attain the same PL spectra of samples before and after bonding. The PL spectra of glue bonding samples can achieve this goal due to its low annealing temperature. And the measurement results will be shown in chapter4. Figure3-3-4 is the glue bonding sample after removing the substrate and etching stop layer. The surface of sample is mirror-like and this is the ideal result for all bonding methods. The non-uniformity of surface in figure3-3-4 may be caused by the particles in etching process.



Figure3-3-4. A picture of the sample after glue bonding to DBR.

### 3-4. Process for Direct Bonding

The epitaxial structure for wafer bonding process is shown in figure3-4-1. The active layer is consisted of four compressively strained InGaAsP QWs separated by three unstrained InGaAsP barriers. The 40 nm InGaAs etching stop layer is used to stop the HCl wet etching and the peak emission wavelength is centered at 1550 nm. This long-wavelength laser can be used as the source of optical communication system.

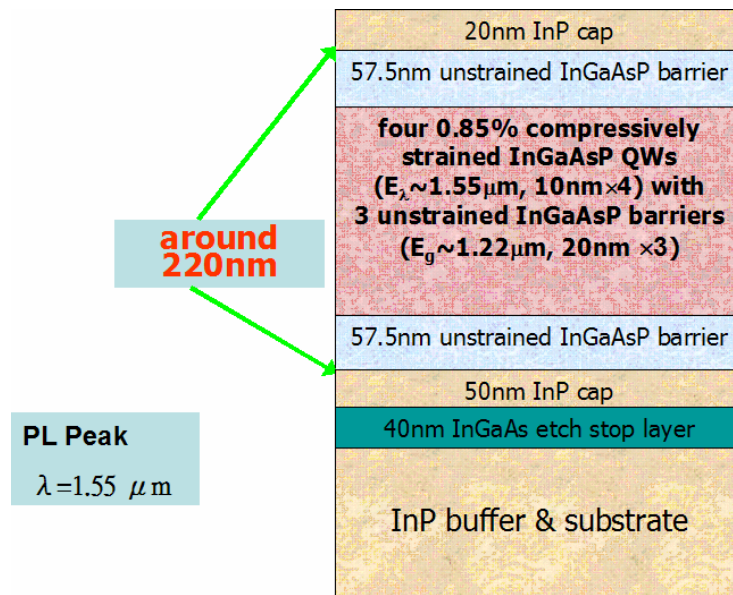


Figure3-4-1. The epitaxial structure for wafer bonding process.

The first step is the clean process which is an important factor to the quality of experiments. All matters including clamping, containers, fixture, and wafers are vibrated with acetone. But be careful that the degree of vibration should be slight because the InP materials are easy to be cracked. After the clean process, two wafers are put together face to face in the water. They will contact each other closely by Van der Waals force and become a block sample. Then we clip the block sample on the bonding fixture and put it into the annealing

chamber. The configurations of the bonding fixture and the annealing chamber are shown in figure3-4-2 (a) and (b).

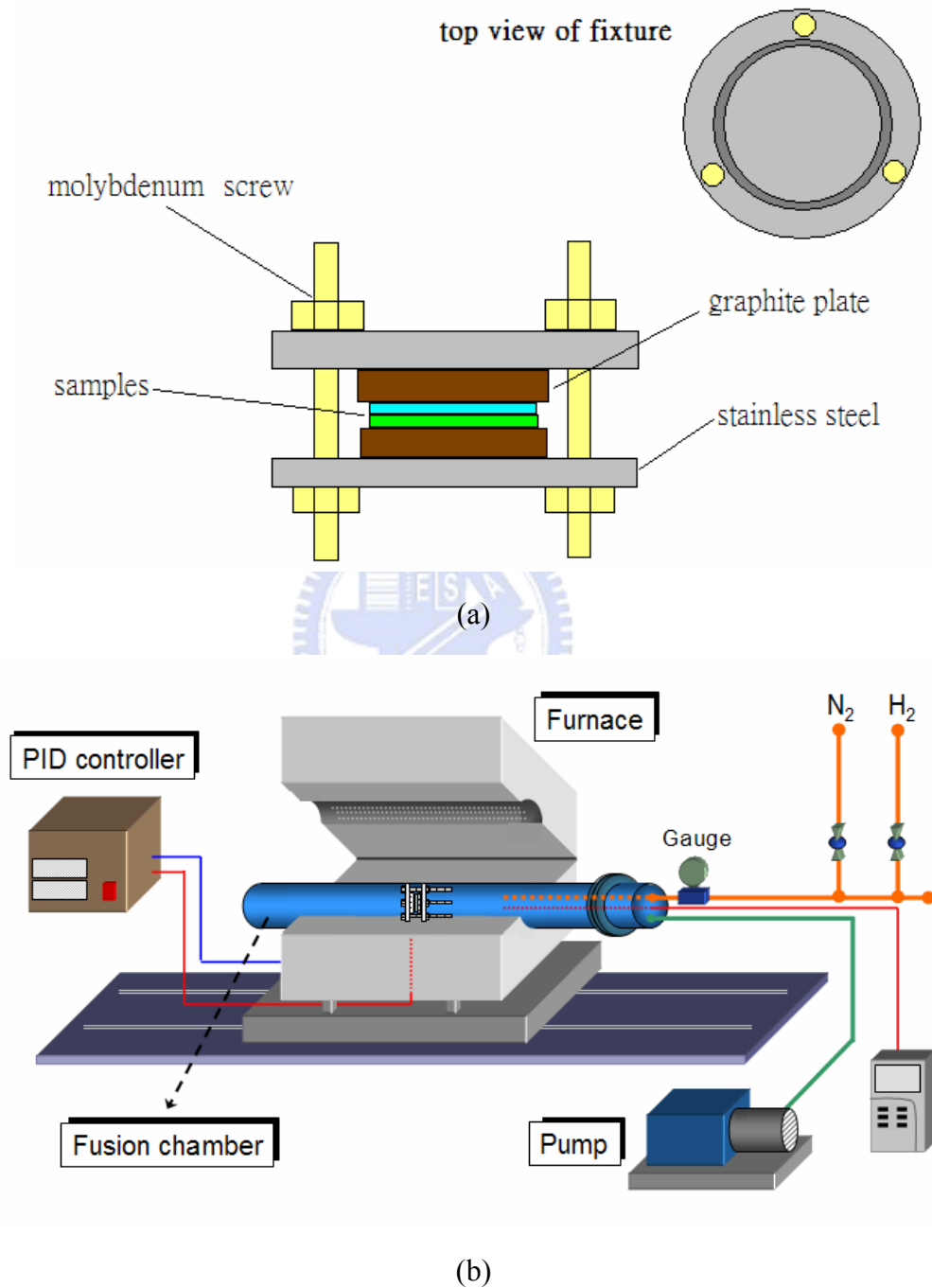


Figure3-4-2. (a) The bonding fixture is composed of molybdenum materials, stainless steels, and graphite plates. (b) The fusion system is composed of chamber, pump, and PID controller.

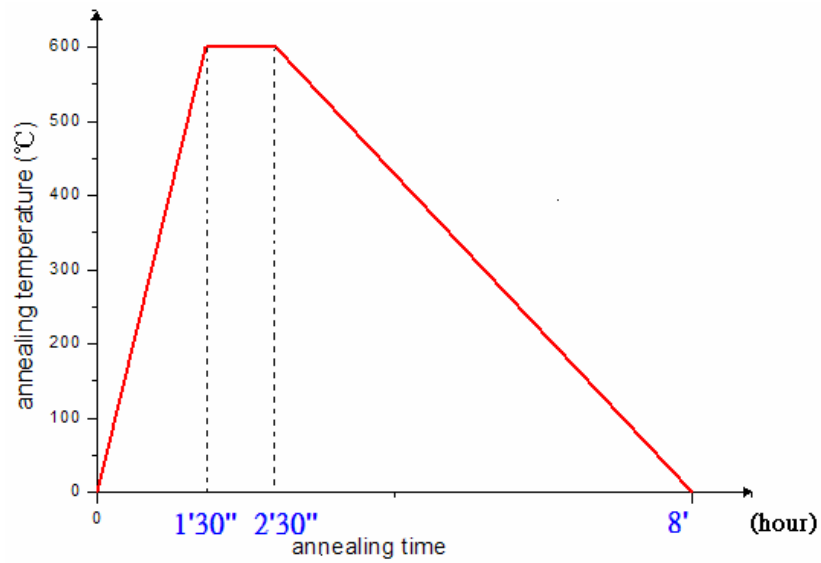
The principle of wafer bonding process is utilizing the different thermal expansion coefficients of stainless steel and molybdenum material to develop the pressure. The thermal expansion coefficients of these two materials at different temperatures are listed in table3-4-1.

Table3-4-1. The thermal expansion coefficients of stainless steel and molybdenum material at different temperatures.

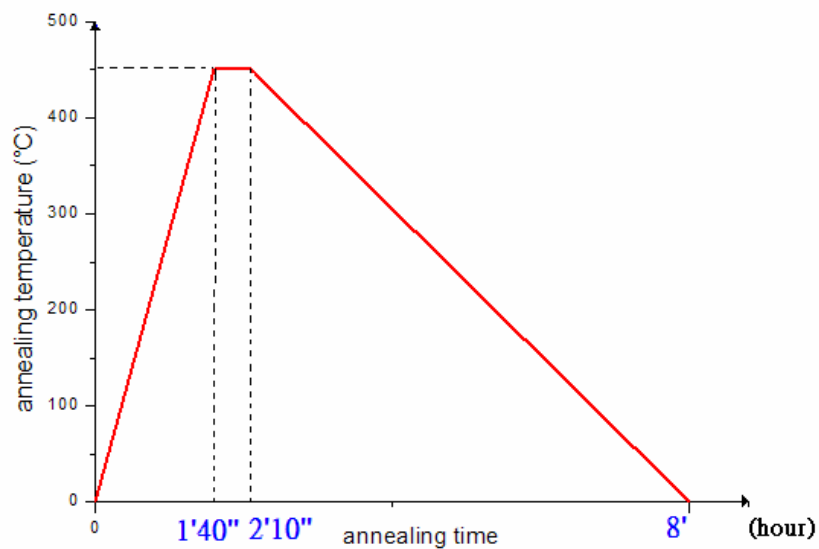
Materials\temperature	373K	600K	800K	1000K
Molybdenum (Mo)	5.42	5.82	6.2	6.71
Stainless steel	17.2	17.8	18.4	19.3

The interface of two wafers will have a chemical reaction to form the atomic covalent bonds due to the high temperature and high pressure conditions. The pressure developed by different thermal expansion coefficients is up to several MPa during the wafer bonding process. The reason we use the graphite plate as the sample clipping is to prevent the bonding reaction between sample and stainless steel.

The sample with fixture is annealed in the furnace. In the process of bonding to DBR, the sample is heated to 600°C in 90 minutes and held at that temperature for 60 minutes with a hydrogen atmosphere to prevent the occurring of native oxide. But in order to clean the annealing furnace and clarify the bonding atmosphere, the argon flow is injected followed by a pumping action twice. If there is no clarification process, the native oxide will be developed and the surface reconstruction will take place on two surfaces of wafers to reduce the surface energy. As a result, the bonding strength will be affected. When the two wafers are close enough, new chemical bonding reaction is formed. The curves of annealing temperature with annealing time in DBR-bonding and sapphire-bonding are shown in figure3-4-3(a) and (b), respectively.



(a)



(b)

Figure3-4-3. The thermal curves of annealing procedure in (a) DBR-bonding and (b) sapphire-bonding.

### 3-5. Key Issues in Wafer Bonding Process

#### 3-5-1. Smoothness of Wafer Surface

Unsmooth wafer surface will lead to the formation of unbonded areas caused by voids and defects at the fusion interface [44]. The unsmooth surface may be caused by particles or

wafer itself. It will result in the rainbow effect as shown in figure3-5-1. However, there are un-flat areas on the edge of the wafers grown by MOCVD. It is necessary to avoid using the edge part of the wafer.

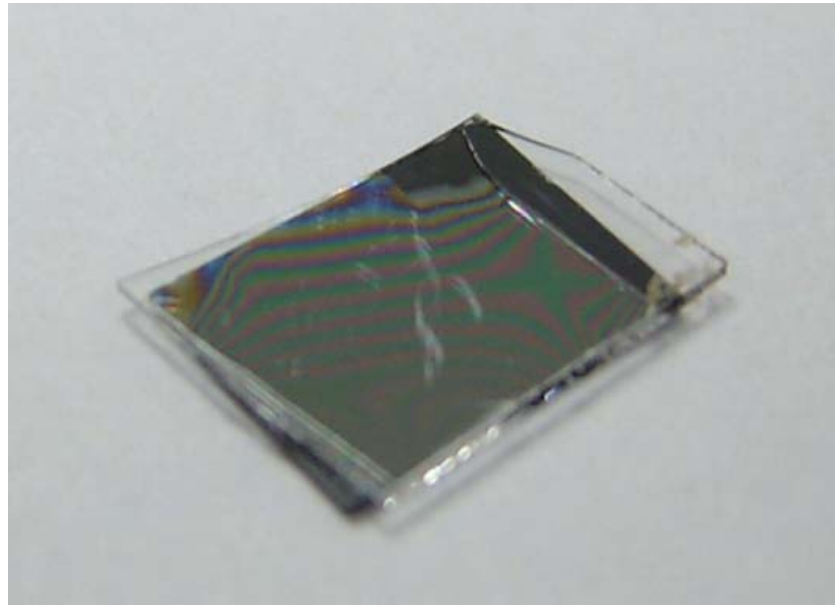


Figure3-5-1. The rainbow effect is caused by unsmooth wafer surface.

### 3-5-2. III-V Oxide on Wafer Surface

III-V oxide on the wafer surface will lead to the formation of bubbles or tent-like structure at bonding interface. Figure3-5-2 shows the bubbles on the sample. The bubbles can be avoided by introducing the channel patterns. Before adhering two wafers, the photolithography process is practiced to define the channel patterns. The width of each channel and the distance between channels are  $10\ \mu\text{m}$  and  $100\ \mu\text{m}$ . The channels are used to drain the steam from the III-V oxide and reduce the appearance of bubbles.

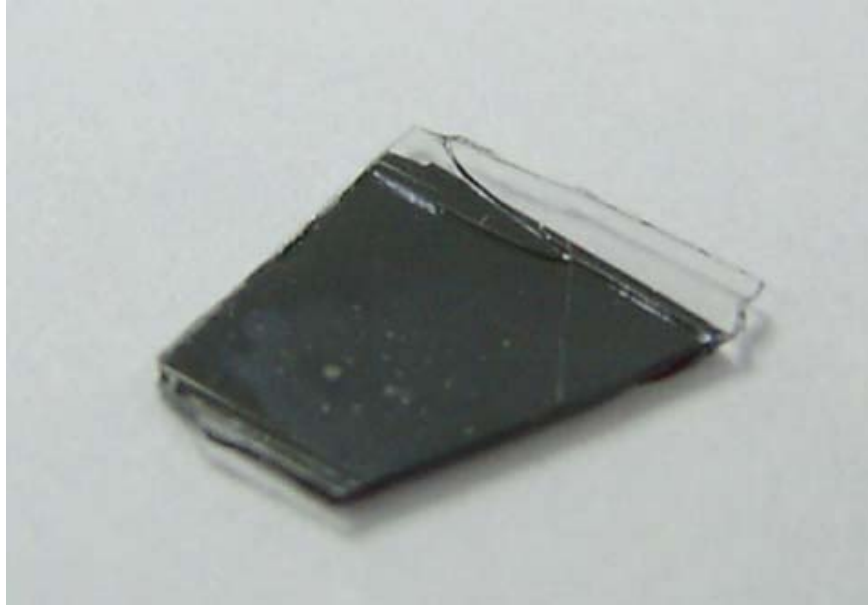


Figure3-5-2. The bubbles at the interface will affect the uniformity of wafer bonding.

### 3-5-3. Annealing Atmosphere

Annealing atmosphere of direct bonding process affects the characteristics of bonding samples. The air, nitrogen, argon, hydrogen, or reductant atmosphere (10% hydrogen + 90% nitrogen) is often adopted in most bonding experiments [45]. The samples are oxidized in air due to oxygen. In order to obtain a better quality of bonding process, the inactive gas like nitrogen, argon or reductant atmosphere is used to prevent the development of oxide. If we use the wrong gas in bonding process, the quality of bonding will be affected greatly as shown in figure3-5-3. In our experiments the gas of hydrogen is used to take the role of reductant at 1 atm.

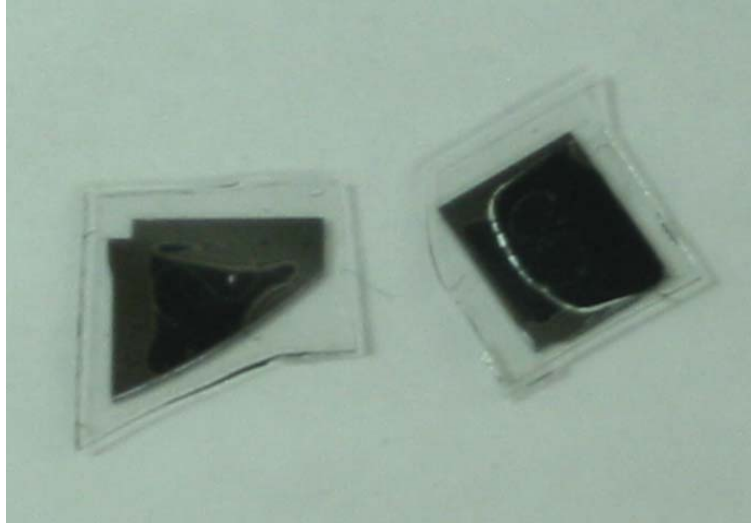


Figure3-5-3. Using the gas of argon as atmosphere makes the bonding process fail.

#### **3-5-4. Uniform Pressure**

In the bonding process, the pressure is applied on wafers to make the atoms of two wafer surfaces contact each other and form chemical bonds. Nonuniform pressure might cause un-uniform fused areas or even un-fused areas at the fusion interface. As a result, the flatness of surfaces of the stainless steel discs and graphite plates should be checked before the process. The graphite plates should be ground into flatness before clipping the sample. Another factor is that the power exerted on the molybdenum screws needs to be applied one by one gradually to provide uniform pressure on sample.

#### **3-5-5. Sample Size**

The size of sample directly affects the pressure exerted on the sample. When the sample is large, the pressure exerted on the unit area is small. As a result, the pressure is affected not only by the annealing temperature and annealing time but also by the sample size. The factor of sample size is often easy to be ignored. If the sample size is too small, the diffusion at the



interface will be more serious by the reason of over-pressure and MQWs may be destroyed. The star-shape texture on the substrate surface is shown in figure3-5-4. And figure3-5-5 shows the texture on the active layer after removing the substrate and etching stop layer. The destruction of MQWs caused by diffusion occurs from the edge to the center of sample.

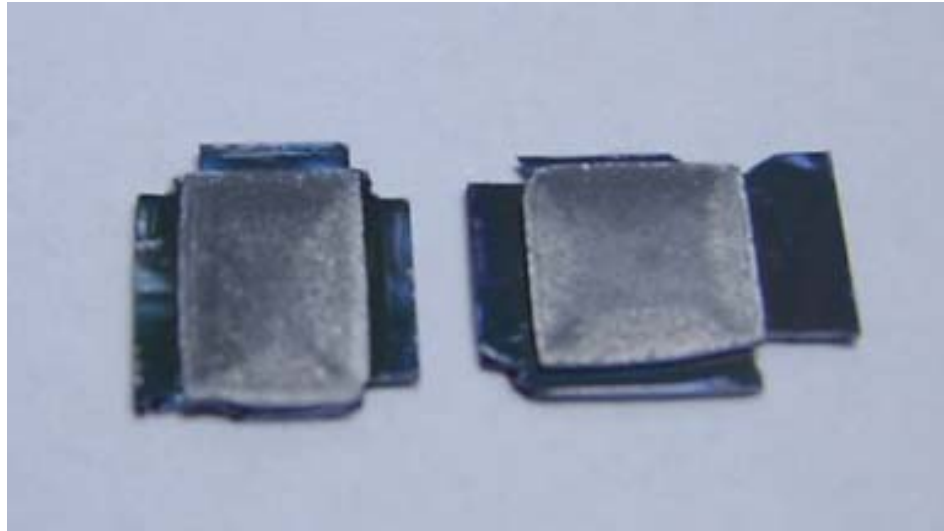


Figure3-5-4. The star-shape texture on the surface of substrate.



Figure3-5-5. The texture destroys the QW structure by diffusion.

In our experiment, the size of one centimeter square is employed. However, there is a shortcoming of large-size sample when channels are fabricated to prevent the appearance of

bubbles. In the process of annealing, the thermal stress will concentrate on the defects of surface, so the sample is even much easier to crack along the channels. In other words, the large-size samples will become more fragile.

### **3-5-6. Wafer Structure**

The wafer structure also affects the bonding quality of samples. Because of the diffusion effect at the bonding interface, the InP cap layer should be introduced to the bonding structure to reduce the diffusion effect.

### **3-6. Substrate Removal**

The last step is to remove the substrate. The InP substrate is removed by HCl solution and then the etching stop layer is removed by H<sub>2</sub>SO<sub>4</sub> solution. The etching rate of stop layer is 0.4  $\mu$  m/min and the color variation of surface can be observed as the sample immersed in the solution. A little over-etching should be practiced to totally remove the residual InGaAs layer. Otherwise, the PL spectrum will be inaccurate. After the substrate removal process we should see a flat and mirror-like surface.

### **3-7. Conclusions**

The fabrication process of two-dimensional photonic crystal defect cavities bonded to sapphire is illustrated in figure3-7-1. The ideal bonding procedure should consist of critical clean process, suitable sample size, enough bonding pressure with high uniformity, low annealing temperature, and the right atmosphere and wafer structure with enough thickness of cap layer.

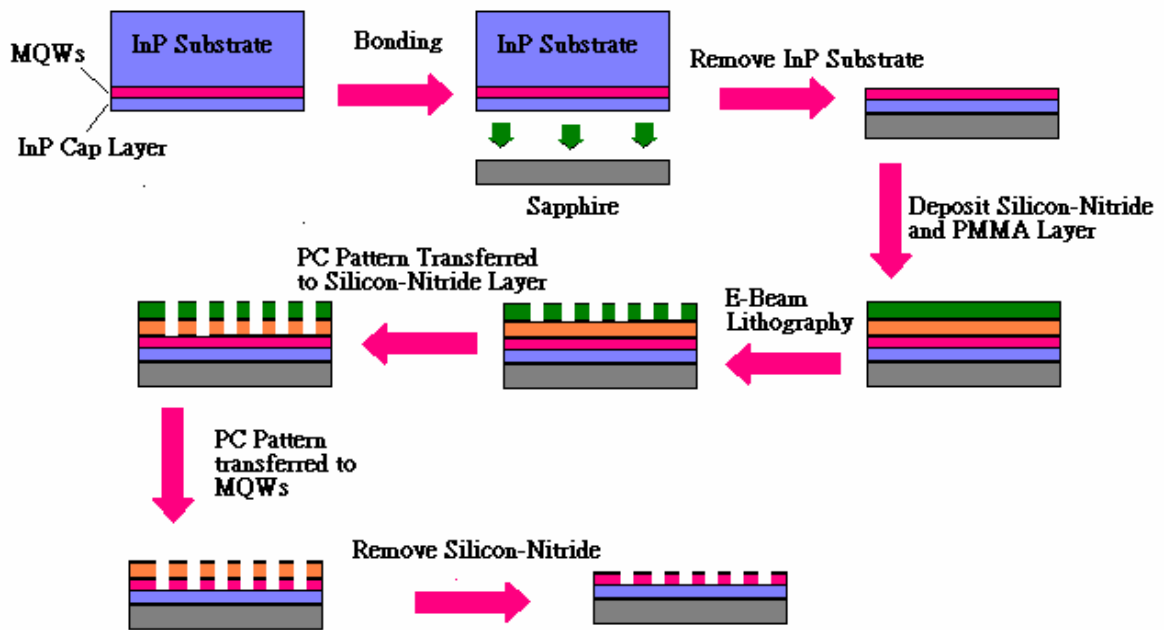


Figure3-7-1. The complete fabrication process of two-dimensional photonic crystal defect cavities bonded to sapphire.

## Chapter4. Measurement Results

### 4-1. Patterns Designed

There are three popular numerical analysis methods of calculating the photonic band structures, plane-wave expansion method (PWE), transfer-matrix method, and finite-difference time-domain method (FDTD). Here we use the “R-soft” software to simulate the designed structures which uses PWE method to calculate the band structures of patterns and FDTD method to perform the lasing mode profiles.

As we design the patterns of PC lasers, we should have a concept that the PC structure directly affects the normalized frequency. The effect factors are  $r/a$  ratio, slab thickness  $d$ , and index contrast, etc. As illustrated for membrane structure, a typical band diagram of TE-like bands with 500nm lattice constant and 0.3  $r/a$  ratio, i.e. 150nm hole radius, is shown in figure4-1-1. In this band diagram, the first band is the so-called “dielectric band” with lower normalized frequency and the second band is the so-called “air band” with higher normalized frequency. There is a forbidden band between the first two bands over all wave vectors below the light line which denotes the interface between the dielectric slab and the air-claddings.

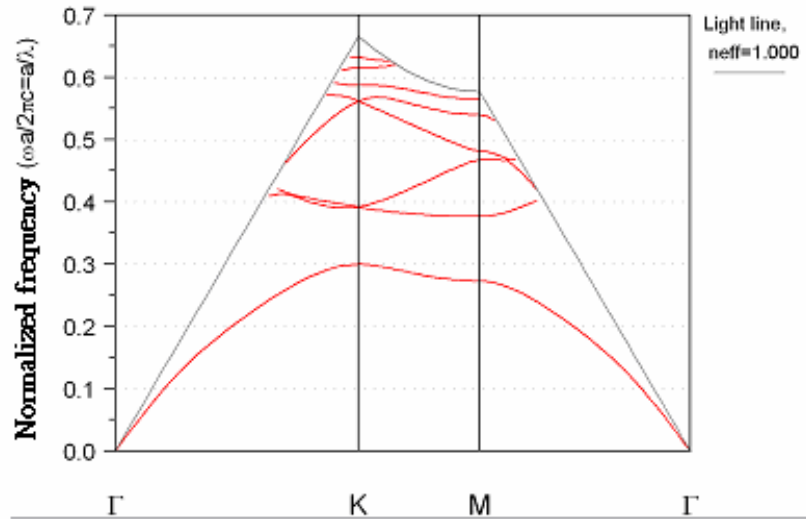


Figure4-1-1. The TE-like band diagram of two-dimensional photonic crystal membrane with 0.3 r/a ratio and 500 nm lattice constant.

As we design a device with asymmetric structure due to the changing of index contrast, the dimensions of patterns should be designed differently from air-cladding structure. For example, the index profile for sapphire-bonded structure is shown in figure4-1-2 and the corresponding band structure is shown in figure4-1-3.

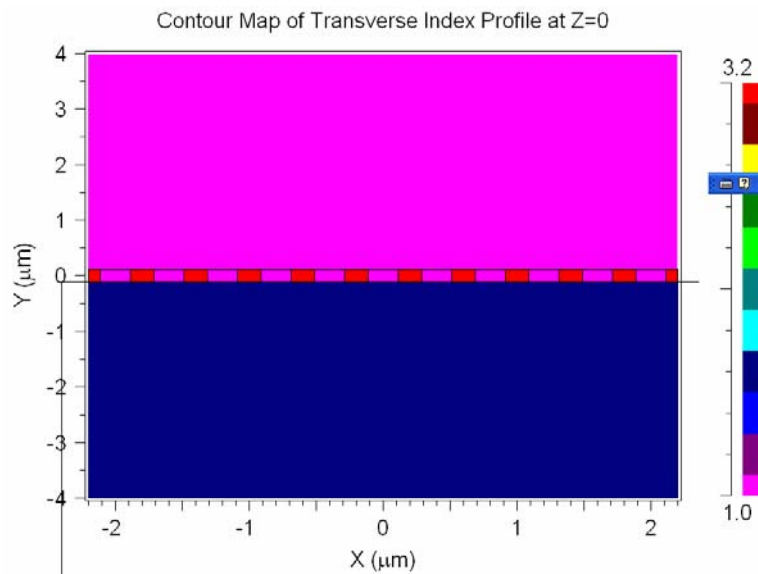


Figure4-1-2. The index profile of the asymmetric photonic crystal slab structure.

From figure4-1-3, it can be noticed that asymmetric photonic crystal slab structure has no complete band gap. And the width of forbidden gap along K-direction to M-direction is about 0.03 in normalized frequency, which corresponds to 150 nm span in wavelength. In order to align the gain peak of MQWs with defect modes because of the changing of index contrast, the designed r/a ratio of patterns should be changed.

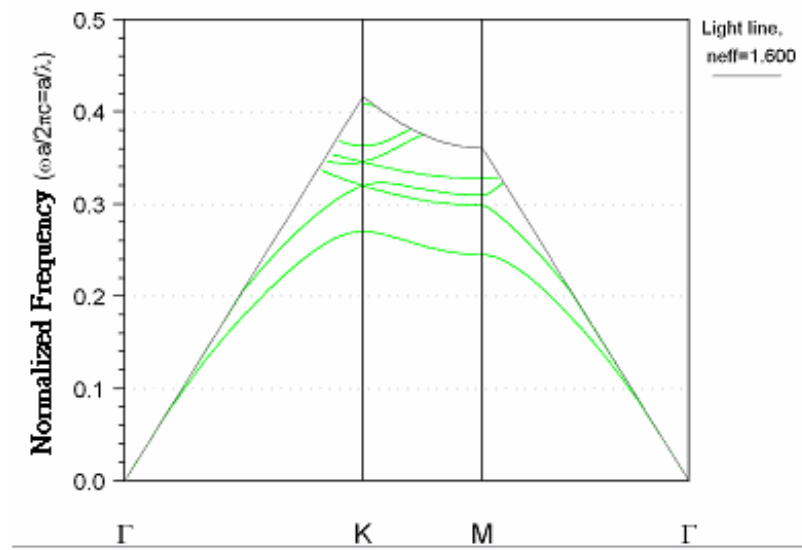


Figure4-1-3. The typical band diagram of asymmetric photonic crystal slab with 400nm lattice constant and 0.28 r/a ratio.

## 4-2. Measurement Results

In order to measure material characteristics and the characteristics of two-dimensional photonic crystal lasers, a micro-photo-luminescence (PL) system with sub-micro-scale resolution in microscope and sub-nano-scale resolution in spectrum is necessary. The simple configuration and photo of our micro-PL system are shown in figure4-2-1. In this system, an 845 nm TTL laser is used as the pump source. This TTL laser can be used both under pulse

operation and continuous-wave operation. Here the pulse operation is practiced in our devices.

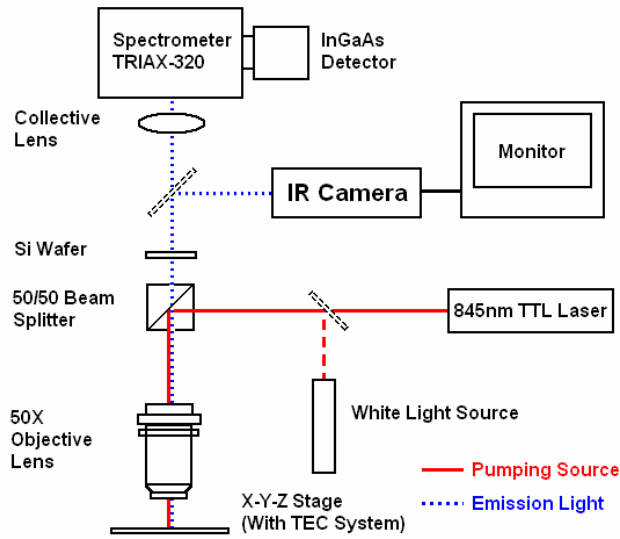


Figure4-2-1. The configuration of our micro-photo-luminescence system.

The PL spectra for glue bonding samples are shown in figure4-2-2. Because of the heating problem of glue, we can just apply the results of glue bonding as the goal for direct bonding results. Figure4-2-2 shows the characteristics of the MQWs after glue bonding process. The PL intensity of MQWs for DBR-bonding sample is enhanced. The blue shift of PL spectrum for sapphire-bonding sample can be observed.

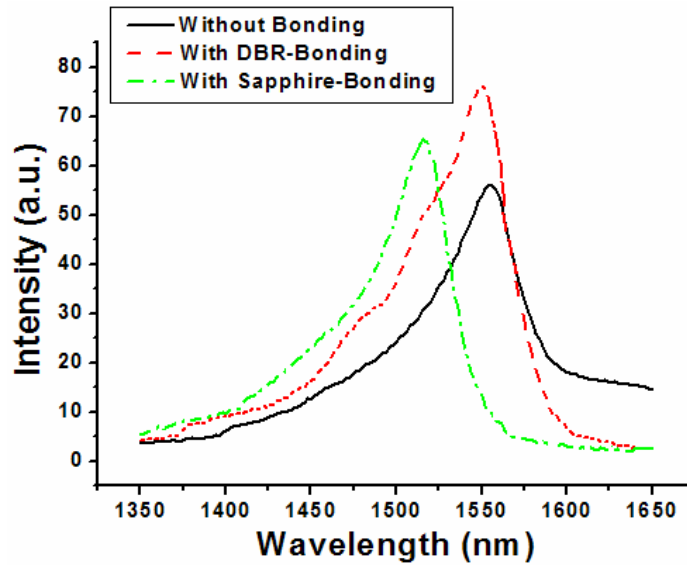
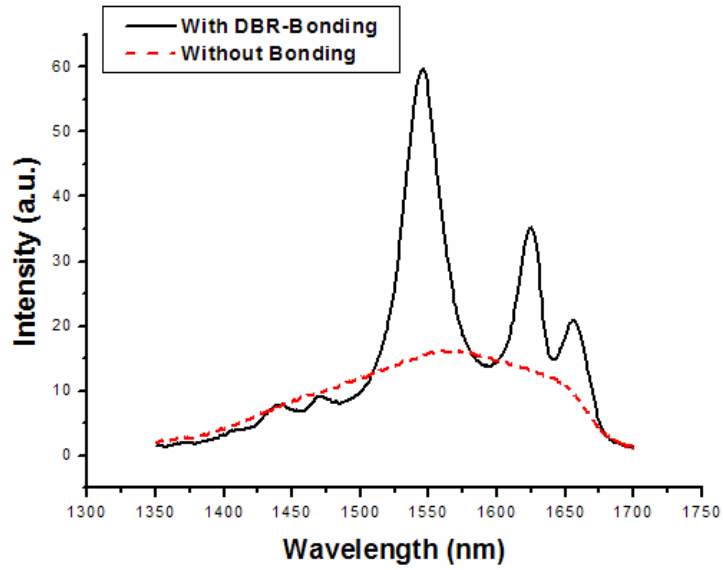


Figure4-2-2. Comparison of glue-bonding samples.

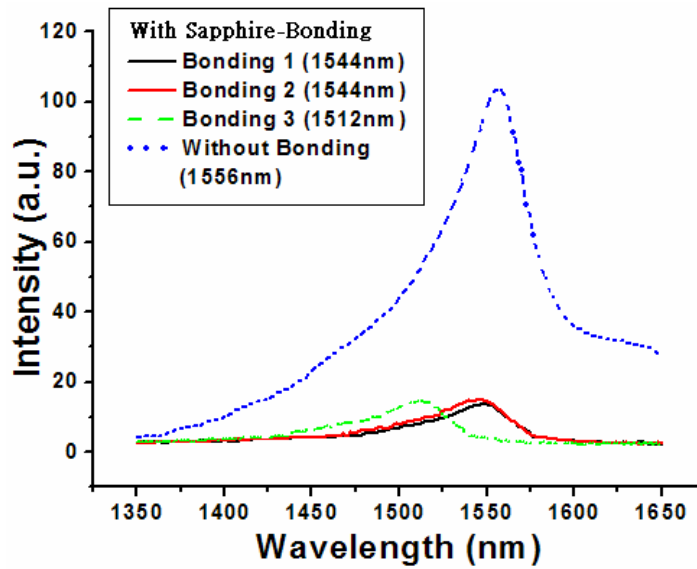
About the results of direct bonding samples, the PL spectra of MQWs direct bonded to DBR and sapphire are shown in figure4-2-3(a) and (b). The trends of direct bonding results are similar to the glue bonding samples. Because the MQWs we used in the experiments are different so the PL spectra are not all the same. From figure4-2-3(a), the PL intensity of MQWs for direct DBR-bonding sample has three gain peaks. After finishing the direct bonding process the intensity of MQWs is enhanced.

And from figure4-2-3(b), compared to the result of glue bonding, the effect of blue shift is similar. But due to the problem of wafer structure, the intensity of spectra for direct bonding sample is reduced. It is because that the MQWs have already been destroyed by diffusion effect in annealing process. The wafers with enough-thickness cap layer can solve this problem.





(a)



(b)

Figure4-2-3. The PL spectra of direct bonding samples which are bonded to (a) DBR and (b) sapphire.

At last, we measure our membrane devices using the micro-PL system. The lattice constant of the measured device is 510nm with  $r/a$  ratios from 0.33 to 0.34. The pump condition is 0.5 MHz with 1.25% duty cycle. One typical lasing spectrum is shown in figure4-2-4.

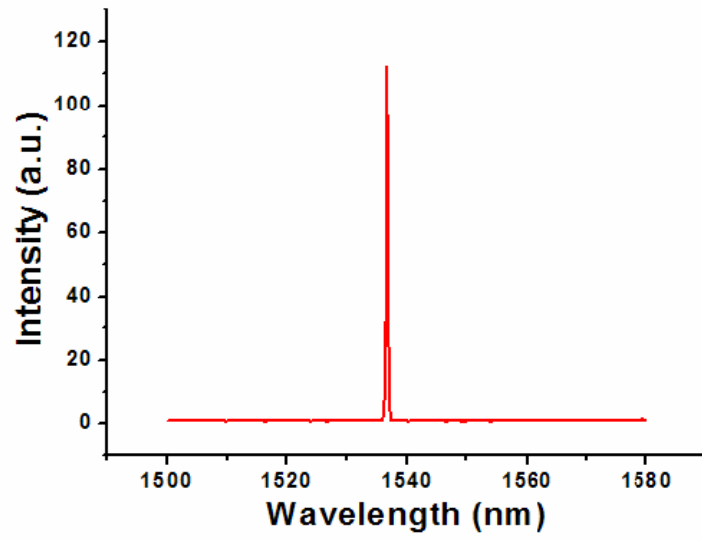


Figure4-2-4. The spectrum shows that the lasing wavelength is at 1538nm.



## Chapter5. Conclusions

In this thesis, we develop the fabrication of two-dimensional photonic crystal membrane lasers. It is the basic device for high index contrast structure. It is believed that continuous-wave operation or even electrically-driven operation can be achieved by its low optical loss in the future. We also develop the wafer bonding technology and try to integrate the photonic crystal wafer with sapphire and DBR. By this way, it is possible to fabricate a device with both high index contrast and thermal conductivity. It is believed that there will be more and more excellent achievements in the days to come. Photonic crystal is a new man-made photonic material whose optical properties can be designed to fit our needs. And the potential of applications is wide to our nano-life in the future.



## References

- [1] E. Yablonovitch, *Phys. Rev. Lett.*, vol. 58, pp. 2059-2062, 1987.
- [2] J. D. Joannopoulos, R. D. Meade, J. N. Winn, "Photonic Crystals", *Princeton University Press*, 1995.
- [3] O. Painter, R.-K. Lee, A. Scherer, A. Yariv, J. D. O'Brien, P. D. Dapkus, and I. Kim, *Science* vol. 284, pp. 1819-1821, 1999.
- [4] O. Painter, J. Vuckovic, and A. Scherer, *J. Opt. Soc. Amer. B* vol. 16, pp. 275-285, 1999.
- [5] H.-Y. Ryu, H.-G. Park, and Y.-H. Lee, *IEEE J. Select. Topics Quantum Electron.* vol. 4, pp. 891-908, 2002.
- [6] H.-Y. Ryu, S.-H. kim, H.-G. Park, J.-K. Hwang, Y.-H. Lee, and J.-S. Kim, *Appl. Phys. Lett.* vol. 80, pp. 3883-3885, 2002.
- [7] K. hennessy, C. Reese, A. Badolato, C.-F. Wang, A. Imamoglu, G. Jin, S. Shi, and D.-W. Prather, *Appl. Phys. Lett.* vol. 83, pp. 3650-3652, 2003.
- [8] H.-Y. Ryu, J.-K. Hwang, and Y.-H. Lee, *IEEE J. Quantum Electron.* vol. 39, pp. 314-322, 2003.
- [9] M. Loncar, T. Yoshie, A. Scherer, P. Gogna, and Y. Qiu, *Appl. Phys. Lett.* vol. 81, pp. 2680-2682, 2002.
- [10] H.-G. Park, J.-K. Hwang, J. Hoon, H.-Y. Ryu, S.-H. Kim, J.-S. Kim, Y.-H. Lee, *IEEE J. Quantum Electron.* vol. 38, pp. 1353-1365, 2002.
- [11] H.-Y. Ryu, M. Notomi, and Y.-H. Lee, *Appl. Phys. Lett.* vol. 83, pp. 4294-4296, 2003.
- [12] M. Loncar, M. Hochberg, A. Scherer, and Y. Qiu, *Opt. Lett.* vol. 29, pp. 721-723, 2004.

- [13] H.Y. Ryu, Y.H. Lee, R. Sellin, and D. Bimberg, *Appl. Phys. Lett.*, vol. 78, pp. 1174-1176, 2001.
- [14] H.Y. Ryu, J.K. Hwang, and Y.H. Lee, *Phys. Rev. B*, vol. 59, pp. 5463-5469, 1999.
- [15] J.-R. Cao, W. Kuang, Z.-J. Wei, S.-J. Choi, H. Yu, M. Bagheri, J. D. O'Brien, P. D. Dapkus, *IEEE Photon. Technol. Lett.* vol. 17, pp. 941-943, 2005.
- [16] J.-K. Hwang, H.-Y. Ryu, D.-S. Song, I.-Y. Han, H.-K. Park, D.-H. Jang, and Y.-H. Lee, *IEEE Photon. Technol. Lett.* vol. 12, pp. 1295-1297, 2000.
- [17] H.-G. Park, S.-H. Kim, S.-H. Kwon, Y.-G. Ju, J.-K. Yang, J.-H. Baek, S.-B. Kim, and Y.-H. Lee, *Sci.* vol.305, pp. 1444-1447, 2004.
- [18] O. J. Painter, A. Husain, A. Scherer, J. D. O'Brien, OSA, I. Kim, and P. D. Dapkus, *J. of Lightwave Technol.* vol. 17, pp. 2082-2088, 1999.
- [19] O. Painter, R.-K. Lee, A. Scherer, A. Yariv, J. D. O'Brien, P. D. Dapkus, and I. Kim, *Sci.* vol. 284, pp. 1819-1821, 1999.
- [20] Po-Tsung Lee, J. R. Cao, Sang-Jun Choi, Zhi-Jian Wei, John D. O'Brien, and P. Daniel Dapkus, *Photon. Technol. Lett.*, vol. 14, pp. 435-437, 2002.
- [21] H.-Y. Ryu, H.-G. Park, and Y.-H. Lee, *IEEE J. On Selected Topics In Quantumelectronics*, vol. 8, pp. 891-906, 2002.
- [22] R. van der Heijden, E. van der Drift, E.J. Geluk, R.W. van der Heijden, F. Karouta, P.A.M. Nouwens, Y.S. Oei, T. de Vries, and H.W.M. Saleminck, Proceedings of Symposium *IEEE/LEOS*, 2003.
- [23] S.B. Phatak and G. Kelner, *J. Electrochem. Soc. :Solid-State Sci. and Technol.* vol. 126, pp. 287-292, 1979.

- [24] L. A. Coldren, K. Furuya, and B. I. Miller, *J. Electrochem. Soc. :Solid-State Sci. and Technol.* vol. 130, pp. 1918-1926, 1983.
- [25] Q.Y. Tong, U. Gösele, John Wiley & Sons, *Semiconductor wafer bonding: Sci. and Technol.* Inc, 1999.
- [26] G. E. Hofler, D. A. Vanderwater, D. C. DeFevere, F. A. Kish, M. D. Camres, F. M. Steranka, and I.-H. Tan, *Appl. Phys. Lett.* vol. 69, pp. 803, 1996.
- [27] H. C. Lin, K. L. Chang, K. C. Hsieh, K. Y. Cheng, and W. H. Wang, *J. Appl. Phys.* vol. 92, pp. 4132, 2002.
- [28] 以晶圓接合與金屬誘發使非晶矽薄膜結晶,詹俊雄,國立交通大學碩士論文.
- [29] L. Gorden, g. I. Woods, R. C. Eckhardt, R. R. Route, R. S. Feigelson, M. M. Fejer, and R. L. Byer, *Electron. Lett.* vol. 29, pp. 1942, 1993.
- [30] D. J. Olego, Y. Okuno, T. Kawano, and M. Tamuro, *J. Appl. Phys.* vol. 71, p. 4503, 1992.
- [31] D. J. Olego, Y. Okuno, and T. Kawano, *J. Appl. Phys.* vol. 71, p. 4493, 1992.
- [32] L. Lazzarini, G. Attolini, D. Bertone, P. Franzosi, C. Pelosi, and G. Salviati, *Inst. Phys. Conf. Ser.* vol. 134, p. 325, 1993.
- [33] Yae Okunoo, *Appl. Phys. Lett.* vol. 68, p. 2855, 1996.
- [34] <http://ab-initio.mit.edu/atoms/mitite.html>.
- [35] U. Gösele, Y. Bluhm, G. Kästner, P. Kopperschmidt, G. Krauter, R. Scholz, A. Schumacher, St. Senz, and Q.-Y. Tong, *J. Vac. Sci. Technol. A*, vol. 17, pp. 1145-1152, 1999.
- [36] W.H.Ko. "Bonding Techniques for Micro Sensors, Micromachining and Micropackaging of Transducers", *Elsevier Science Publishers*, 1985.

- [37] P. Kopperschmidt, S. Senz, G. Kastner, D. Hesse, and U. M. Gosele, *Appl. Phys. Lett.* vol. 72, p. 3181, 1998.
- [38] Ray-Hua Horng, Yi-Chung Lien, Wei-Chih Peng, Dong-Sing Wu, Chung-Yang Tseng, Chi-Hua Seieh, Man-Fang Huang, Shi-Jen Tsai and Jin-Shiarng Liu, *Jpn. J. Appl. Phys.* vol. 40, p. 2747, 2001.
- [39] P. Kopperschmidt, G. KaÈstner, D. Hesse, N.D. Zakharov, U. GoÈsele, *Appl. Phys. Lett.* vol. 70, p. 2972, 1997.
- [40] G.P. Imthurn, G.A. Garcia, H.W. Walker, L. Forbes, *J. Appl. Phys.* vol. 72, p. 2526, 1992.
- [41] T. Abe, K. Ohki, A. Uchiyama, K. Nakazawa, Y. Nakazato, *Jpn. J. Appl. Phys.* vol. 33 (Suppl. 1B), p. 514, 1994.
- [42] D. Pasquariello and K. Hjort, *IEEE J. On Selected Topics In Quantumelectronics*, vol. 8, p. 118, 2002.
- [43] W. P. Eaton, S. H. Risbud, and R. L. Smith, *Appl. Phys. Lett.* vol. 65, pp. 439–441, 1994.
- [44] M. Shimbo, K. Furukawa, K. Fukuda, and K. Tanzawa, *J. Appl. Physic.*, vol. 60, p. 2987, 1986.
- [45] G. Kastner, O. Breitenstein, R.Scholz, *J.Mater. Sci.* vol. 13, p. 593, 2002.